

Individual Stellar Halos of Massive Galaxies Measured to 100 kpc at $0.3 < z < 0.5$ using Hyper Suprime-Cam

Song Huang,^{1,2*} Alexie Leauthaud,^{2,1} Jenny E. Greene,³ Kevin Bundy,^{4,1}
 Yen-Ting Lin,⁶ Masayuki Tanaka,⁵ Satoshi Miyazaki,^{5,7}
 Yutaka Komiyama^{5,7}

¹*Kavli-IPMU, The University of Tokyo Institutes for Advanced Study, the University of Tokyo, Kashiwa 277-8583, Japan*

²*Department of Astronomy and Astrophysics, University of California Santa Cruz, 1156 High St., Santa Cruz, CA 95064, U.S.A*

³*Department of Astrophysical Sciences, Peyton Hall, Princeton University, Princeton, NJ 08540, USA*

⁴*UCO/Lick Observatory, University of California, Santa Cruz, 1156 High Street, Santa Cruz, CA 95064, USA*

⁵*National Astronomical Observatory of Japan, 2-21-1 Osawa, Mitaka, Tokyo 181-8588, Japan*

⁶*Academia Sinica Institute of Astronomy and Astrophysics, P.O. Box 23-141, Taipei 10617, Taiwan*

⁷*SOKENDAI (The Graduate University for Advanced Studies), Mitaka, Tokyo, 181-8588, Japan*

Accepted XXX. Received YYY; in original form ZZZ

ABSTRACT

Massive galaxies display extended light profiles that can reach several hundreds of kilo parsecs. These stellar halos provide a fossil record of galaxy assembly histories. Using data that is both wide ($\sim 100 \text{ deg}^2$) and deep ($> 28.5 \text{ mag arcsec}^{-2}$ in i -band), we present a systematic study of the stellar halos of a sample of more than 3000 galaxies at $0.3 < z < 0.5$ with $\log M_{\star}/M_{\odot} > 11.4$. Our study is based on high-quality ($0.6''$ seeing) imaging data from the Hyper Suprime-Cam (HSC) Subaru Strategic Program (SSP), which enables us to individually estimate surface mass density profiles to 100 kpc without stacking. As in previous work, we find that more massive galaxies exhibit more extended outer profiles. When this extended light is not properly accounted for as a result of shallow imaging or inadequate profile modeling, the derived stellar mass function can be significantly underestimated at the highest masses. Across our sample, the ellipticity of outer light profiles increases substantially as we probe larger radii. We show for the first time that these ellipticity gradients steepen dramatically as a function of galaxy mass, but we detect no mass-dependence in outer color gradients. Our results support the two-phase formation scenario for massive galaxies in which outer envelopes are built up at late times from a series of merging events. We provide surface mass surface mass density profiles in a convenient tabulated format to facilitate comparisons with predictions from numerical simulations of galaxy formation.

Key words: galaxies: elliptical and lenticular, cD – galaxies: formation – galaxies: photometry – galaxies: structure – galaxies: surveys

1 INTRODUCTION

Simulations of structure formation within the context of the Λ -CDM cosmological model make predictions for the hierarchical growth of dark matter halos and galaxies (e.g. Baugh et al. 1996; De Lucia et al. 2006), but there are many open questions regarding the star-formation history, mass assembly process, and structural evolution of massive galaxies. Massive galaxies are thought to grow according to a “two-phase” formation scenario (e.g. Oser et al. 2010, 2012).

In this scenario, the progenitors of $z \sim 0$ massive early-type galaxies (ETGs) undergo a rapid growth phase at $z \sim 2$ triggered either by disk instabilities or gas-rich mergers (e.g. Hopkins et al. 2008; Dekel et al. 2009). Observationally, the progenitors of ETGs are thought to correspond to the population of massive quiescent galaxies at high redshift that have smaller average effective radii (R_e ; e.g. Trujillo et al. 2006; van Dokkum et al. 2008; Cimatti et al. 2008). These high redshift galaxies also have slightly higher central velocity dispersions and stellar mass densities (μ_{\star} ; e.g. van de Sande et al. 2011; Belli et al. 2014), and more disk-like morphologies (e.g. van der Wel et al. 2011) than low redshift

* E-mail: song.huang@ipmu.jp (SH)

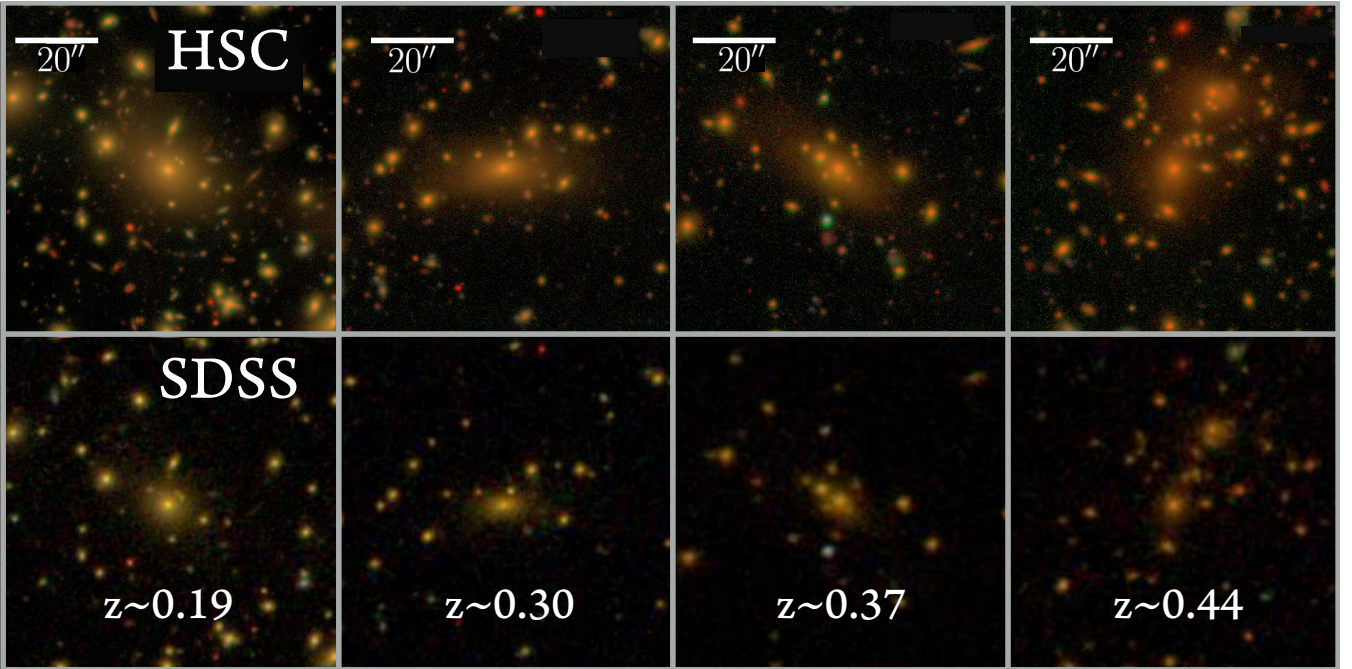


Figure 1. A comparison between the depth and imaging quality of SDSS and the HSC wide layer for a sample of nearby massive elliptical galaxies at $0.2 < z < 0.5$. These images are generated using *gri* band images with an arcsinh stretch (Lupton et al. 2004). The HSC WIDE layer is 3.0-4.0 magnitudes deeper than SDSS. This added depth is critical in order map the outskirts of ETGs out to large radii.

galaxies (e.g. Bezanson et al. 2009; van Dokkum et al. 2010) with similar stellar mass.

Following the initial phase of growth, feedback from stars and/or AGN (e.g. Sijacki et al. 2007; Fabian 2012) efficiently quenches star formation in massive galaxies. A large fraction of these massive progenitors are already quiescent by $z = 1$ (e.g. Bezanson et al. 2009; Kriek et al. 2016). The second phase of their assembly is driven by non-dissipative processes such as dry mergers with other galaxies (e.g. Naab et al. 2006; Khochfar & Silk 2006). The “two-phase” formation of massive galaxies help explain both the observed increase in the effective radii (R_e) of massive galaxies (e.g. Newman et al. 2012; van der Wel et al. 2014) and the build-up of stellar halos (e.g. Szomoru et al. 2012; Patel et al. 2013). It also posits that minor mergers dominate the mass assembly of massive galaxies at late times (e.g. Hilz et al. 2012, 2013; Oogi & Habe 2013; Bédorf & Portegies Zwart 2013; Laporte et al. 2013).

Both numerical simulations (e.g. Oser et al. 2010) and semi-analytic models (SAM; e.g. Lee & Yi 2013, 2017) agree that the mass fraction in the accreted component should increase with total galaxy stellar mass (e.g. Lackner et al. 2012; Cooper et al. 2013; Qu et al. 2017). For instance, recent results from the Illustris¹ simulation (Vogelsberger et al. 2014, Genel et al. 2014) predict that the fraction of accreted stars increases significantly and reaches $f_{\text{accreted}} > 0.5$ at $\log(M_*/M_\odot) > 11.5$ (Rodríguez-Gomez et al. 2016)².

¹ <http://www.illustris-project.org/>

² The Illustris simulation does not reproduce the observed stellar mass function at high M_* end.

Given the success of this two-phase scenario in explaining trends like overall size growth, it is time to confront this model with additional observations, in particular, the detailed surface mass density profiles of low redshift massive galaxies. Early studies based on one-dimensional light profiles found that the surface mass density profiles of nearby ETGs are well described by single-Sérsic profiles (e.g. Kormendy et al. 2009; except for the most central region) and that the Sérsic index increases with total luminosity (e.g. Graham 2013). However, recently, detailed empirical comparison of surface brightness profiles revealed a more complicated situation showing that ETGs belong to two families, those that follow single-Sérsic law, versus those that significantly deviate from the single-Sérsic profile (Schombert 2015). Two-dimensional analyses have also found that the stellar distributions of massive ETGs are often better fit by multiple-component models (e.g. Huang et al. 2013a; Oh et al. 2017). Huang et al. (2013b) further suggest a connection between the multi-component nature of massive galaxies and their two-phase assembly history. To further confront the two-phase scenario requires very deep observations of large samples of massive ETGs to correctly estimate their total stellar masses (e.g. Bernardi et al. 2013; D’Souza et al. 2014) as well as to quantify the amplitude and scatter among outer envelopes (e.g. Capaccioli et al. 2015; Iodice et al. 2016, 2017).

Until now, studies of the surface brightness or mass density profiles of massive galaxies have been either conducted using large samples but with shallow imaging, for example the Sloan Digital Sky Survey (SDSS; e.g. Abazajian et al. 2009; Alam et al. 2015a), or with deeper imaging but much smaller sample sizes (e.g. Gonzalez et al. 2005). In this pa-

per, we take advantage of new high-quality (median seeing of FWHM \sim 0.6'' in *i*-band) and deep (*i*-band surface brightness limit > 28.5 mag arcsec $^{-2}$) images from the Hyper Suprime-Cam (HSC) Subaru Strategic Program (SSP, Aihara et al. 2017a) to characterize the light profiles of massive galaxies out to 100 kpc. The deep imaging depth and excellent seeing conditions of HSC images make them ideal for mapping the M_{\star} distributions of massive galaxies out to very large radii. We select a large sample (~ 7000) of massive central galaxies at $0.3 < z < 0.5$ using ~ 100 deg 2 of data from the HSC wide layer.

In this paper, we use this sample to (a) reliably estimate individual surface mass density (μ_{\star}) profiles of massive galaxies out to 100 kpc, (b) investigate the dependence of their outer stellar halos on total stellar mass, and (c) examine the implications in terms of evaluating the high mass end of the galaxy stellar mass function (SMF). In a second paper in this series, we will investigate the environmental (dark matter halo mass) dependence of the sizes of massive ETGs (Huang et al. in prep.).

This paper is organized as follows. § 2 presents our data and initial sample selection. § 3 describes our procedure for extracting 1-D surface brightness profiles. § 4 describes how we estimate stellar mass. § 5 summarizes the final sample selection procedure. Our main results are presented in § 6 and discussed in § 7. § 8 presents our summary and conclusions.

Magnitudes use the AB system (Oke & Gunn 1983), and are corrected for Galactic extinction using calibrations from Schlafly & Finkbeiner (2011). In this work, we assume $H_0 = 70$ km s $^{-1}$ Mpc $^{-1}$, $\Omega_m = 0.3$, and $\Omega_{\Lambda} = 0.7$. Stellar mass is denoted M_{\star} and has been derived using a Chabrier Initial Mass Function (IMF; Chabrier 2003).

Halo mass is defined as M_{200b} as $M_{200b} \equiv M(< r_{200b}) = 200\bar{\rho} \frac{4}{3}\pi r_{200b}^3$ where r_{200b} is the radius at which the mean interior density is equal to 200 times the mean matter density ($\bar{\rho}$).

Finally, we emphasize that in this work, we do not attempt to disentangle the galaxy light from any ‘‘intra-cluster’’ light component (ICL; e.g. Carlberg et al. 1997; Lin & Mohr 2004; Gonzalez et al. 2005; Mihos et al. 2005). Although the rising stellar velocity dispersion in the outskirts of massive brightest cluster galaxy (BCG) hints at a kinematically separated ICL component (e.g. Dressler 1979; Carter et al. 1999; Kelson et al. 2002; Bender et al. 2015; Longobardi et al. 2015), it is extremely difficult to reliably isolate them photometrically. Moreover, both the stellar halo of main galaxy and the ICL component carry important information regarding the assembly history of central galaxy and its dark matter halo. Therefore, we adopt the view that the light of the main galaxy and the ICL component trace different scales of a single, smooth, and continuous distribution.

2 DATA AND SAMPLE SELECTION

2.1 The Hyper Suprime-Cam Survey

The Subaru Strategic Program (SSP, Aihara et al. 2017b,c) makes use of the new prime-focus camera, the Hyper Suprime-Cam (HSC; Miyazaki et al. 2012, Miyazaki in prep.), on the 8.2-m Subaru telescope at Mauna Kea.

The ambitious multi-layer HSC survey takes advantage of the large field of view (FoV; 1.5 deg in diameter) of this camera and will cover > 1000 deg 2 of sky in 5 broad bands (*grizy*) to a limiting depth of $r\sim 26$ mag in the WIDE layer. This work is based on the internal data release S15B, which covers ~ 110 deg 2 in all 5-band to full WIDE depth. The regions covered by this release overlap with a number of spectroscopic surveys (e.g. SDSS/BOSS: Eisenstein et al. 2011, Alam et al. 2015b; GAMA: Driver et al. 2011, Liske et al. 2015). S15B release has similar sky coverage with the Public Data Release 1 (Please see Table 3 in Aihara et al. 2017c for detailed comparison).

The HSC WIDE survey is about 3.0-4.0 magnitudes deeper in terms of the *i*-band surface brightness limit than SDSS. Combined with the excellent imaging resolution (the median *i*-band seeing is 0.6'') and the wide area, the HSC survey represents an ideal dataset to perform statistical studies of the surface brightness profiles of massive galaxies out to their distant outskirts. Fig 1 illustrates the quality of HSC imaging compared to SDSS for three low redshift ETGs, and shows that HSC survey data are well suited for mapping the stellar distribution of massive galaxies out to large radii.

HSC *i*-band images typically have the best seeing compared to other bands because of strict requirements driven by weak lensing science. We will therefore use *i*-band images to measure the stellar distributions of massive galaxies.

2.2 HSC Data Processing

The full details of the HSC data processing can be found in Bosch et al. (2017) and are briefly summarized here. The HSC SSP data are processed with `hscPipe` 4.0.2, a derivative of the Large Synoptic Survey Telescope (LSST) pipeline (e.g. Jurić et al. 2015; Axelrod et al. 2010), modified for HSC. `hscPipe` first performs a number of tasks at the single exposure level (bias subtraction, flat fielding, background modeling, object detection and measurements). Astrometric and photometric calibrations are performed at the single exposure level. `hscPipe` then warps different exposures on to a common World Coordinate System (WCS) and combines them into coadded images. At this stage, `hscPipe` updates the images with a better astrometric and photometric calibration using stars that are common among exposures.

The pixel scale of the combined images is 0.168''. Photometric calibration is based on data from the Panoramic Survey Telescope and Rapid Response System (Pan-STARRS) 1 imaging survey (Schlafly et al. 2012, Tonry et al. 2012, Magnier et al. 2013). To achieve consistent deblending and photometry across all bands, `hscPipe` performs multi-band post-processing at the `coadd` level. First, `hscPipe` performs object detection on `coadd` images in each band independently and records the flux peak and the above-threshold region (referred as a `footprint`) for each source. Next, `footprints` and peaks from different bands are merged together before performing deblending and measurements. Finally, `hscPipe` selects a reference band for each object based on the *S/N* in different bands (for most galaxies in this work, the reference band is the *i*-band). After fixing the centroids, shape, and other non-amplitude parameters of each object in this reference catalog, `hscPipe` performs forced photometry on the `coadd` image in each band. This forced photometry approach

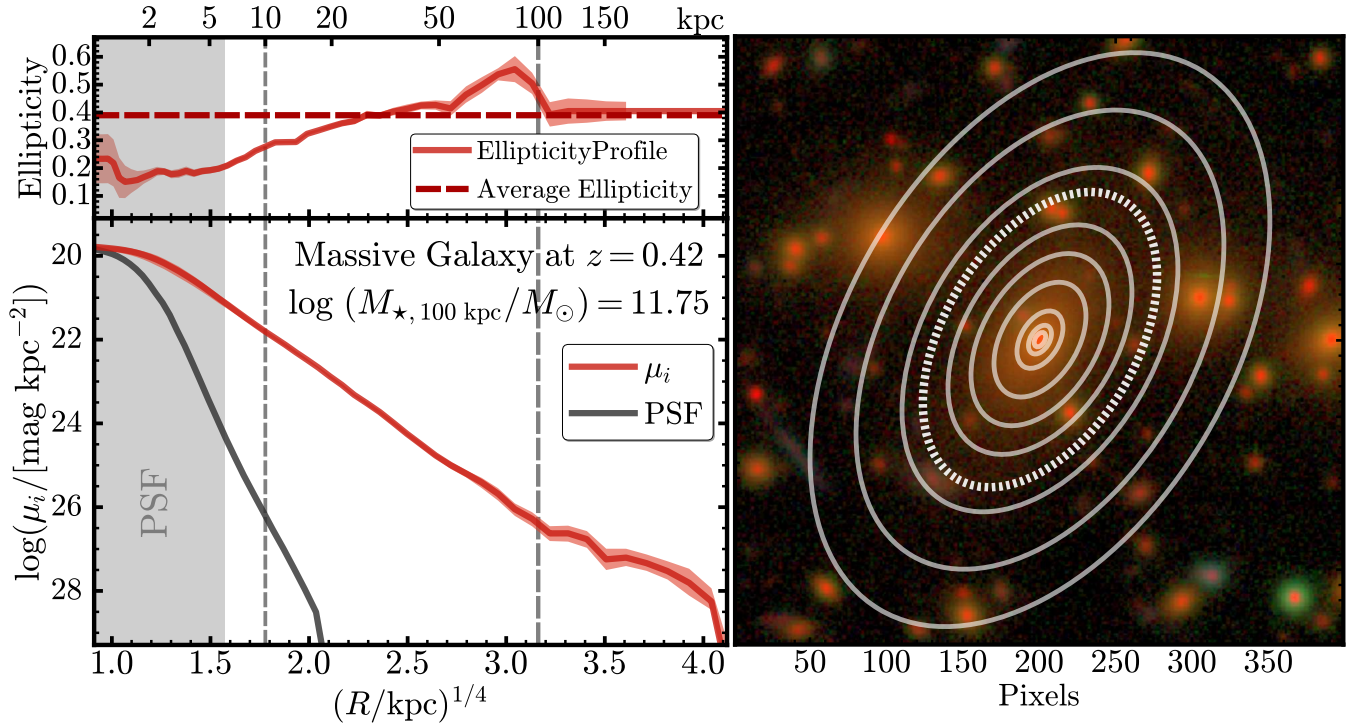


Figure 2. Left: example of the 1-D surface brightness and ellipticity profile of a massive galaxy at $z = 0.23$ in the i -band extracted using `Ellipse`. In this work, we always show the radial profile using a $R^{1/4}$ scaling on the x-axis. By using this scale, the de Vaucouleurs profile will appear as a straight line on this figure. We also plot the relative brightness profile of the PSF model normalized at the central surface brightness of the galaxy to highlight the region most strongly affected by seeing. The grey shaded region highlights the region ($r < 6$ kpc) that is equivalent to twice the size of the half-width of a $1''$ seeing at $z \sim 0.5$. It is a very conservative estimate of the region that we can not reliably extract 1-D profile due to the smearing effect of seeing. On the top panel, the dashed line shows the mean ellipticity used for the final isophote. Right: the three color image of this galaxy with isophotes extracted by `Ellipse`. The thick dotted line highlights the isophote with $\mu_i \sim 28.5$ mag arcsec $^{-2}$.

is optimized to yield accurate galaxy colors at $i_{\text{cModel}} \leq 25.0$ mag (see [Huang et al. 2017](#)).

For each galaxy, `hscPipe` measures a `cModel` magnitude using an approach that is similar to SDSS ([Bosch et al. 2017](#)). However, as opposed to SDSS, the HSC `cModel` is based on forced multi-band photometry which means that it can accurately measure both the *fluxes and colors of galaxies*. The HSC `cModel` algorithm fits the flux distribution of each object using a combination of a de Vaucouleur and an exponential component and accounts for the PSF. The performance of this algorithm has been tested using synthetic objects ([Huang et al. 2017](#)), and the results indicate that, generally speaking, the HSC `cModel` photometry is accurate down to $i > 25.0$ mag. However, `cModel` currently systematically underestimates the total fluxes of massive ETGs with extended stellar distributions. This is caused by an intrinsic limitation of `cModel` as it is incapable of modeling profiles with extremely extended outskirts, a problem that is exacerbated at the depth of the HSC survey. In addition, at the depth of the HSC survey, accurate deblending in the vicinity of large ETGs where satellites and background galaxies often blend with the low surface brightness stellar envelope is a challenging problem. The deblending method currently implemented in `hscPipe` tends to “over-deblend” the outskirts of bright galaxies and leads to an under-estimation of the total flux of massive ETGs (this is discussed further

in [Bosch et al. 2017](#)). For these reasons, our results will be based on custom-developed code to measure the luminosities and stellar masses of massive galaxies. We use the HSC `hscPipe` photometry for two purposes: 1) to perform a first broad sample selection, and 2) to estimate the average color of massive galaxies.

2.3 Initial Massive Galaxy Sample

We begin by using a broad flux cut to select an initial sample of massive galaxies at $z < 0.5$ from the HSC photometric catalog. Based on [Leauthaud et al. \(2016\)](#), $i_{\text{SDSS,cModel}} \leq 21.0$ mag can define a sample that includes almost all $\log(M_{\star}/M_{\odot}) \geq 11.5$ galaxies. We therefore perform an initial conservative selection of massive galaxies with $i_{\text{HSC,cModel}} \leq 21.5$ ³. We also limit our sample to regions that have reached the required depth of the WIDE survey in i -band as defined in [Aihara et al. \(2017c\)](#).

We further select extended objects with no deblending errors, with well defined centroids, and with useful `cModel` magnitudes in all five bands. After removing objects that

³ We neglect small differences between the response curves of the SDSS- i and HSC- i filters.

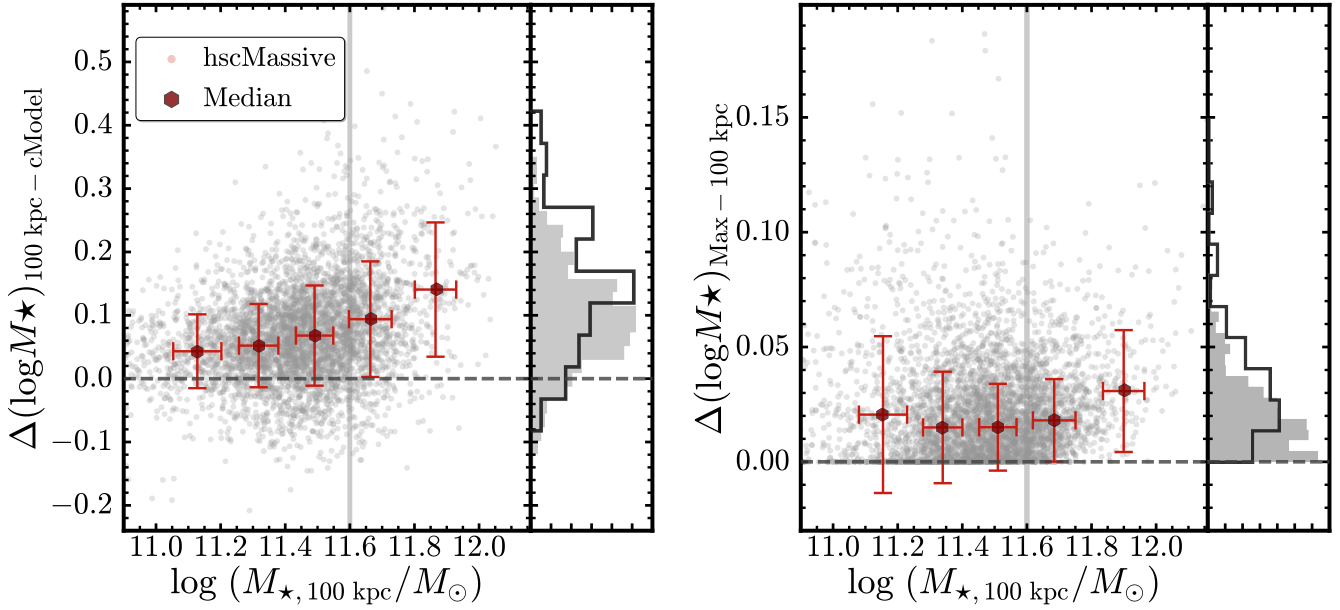


Figure 3. **Left:** Difference between $M_{\star, \text{cModel}}$ and $M_{\star, 100 \text{ kpc}}$ for massive galaxies (grey dots). The running-median of the mass difference is shown by large red hexagons. On average, $M_{\star, \text{cModel}}$ underestimates the total stellar mass of massive galaxies by 0.1 dex while in some cases, the difference can exceed 0.2 dex. Vertical histograms indicate the mass difference for all galaxies (shaded histogram) and for the ones with $\log(M_{\star, 100 \text{ kpc}}/M_{\odot}) > 11.6$ (empty histogram). **Right:** Difference between $M_{\star, \text{Max}}$ and $M_{\star, 100 \text{ kpc}}$ in the same format. The average difference is small (0.02 dex) and with no clear mass-dependence. **Please note that the scales of the vertical axes are different for these two figures.**

have pixels affected by saturation, cosmic-rays, or other optical artifacts⁴, this sample corresponds to 1760845 galaxies and will be referred as **hscPho**.

Here we limit our study to the very high-mass end where the majority of galaxies have either a spectroscopic redshift or a robust red-sequence photo- z from the **redMaPPer** galaxy cluster catalog⁵ (e.g. Rykoff et al. 2014; Rozo et al. 2015b).

We match the **hscPho** sample with a spec- z catalog compiled by the HSC team. It is created by matching HSC objects with a series of publicly available spectroscopic redshifts (e.g. SDSS DR12 Alam et al. 2015a; GAMA DR2 Liske et al. 2015). The spec- z quality flags from different catalogs are homogenized into a single flag that indicates secure redshifts. Please see § 4.4.2 of Aihara et al. (2017c) for details of this catalog. To ensure reasonable M_{\star} -completeness at the high- M_{\star} end we focus on the redshift range $0.3 \leq z \leq 0.5$.

Objects without a spectroscopic redshift are matched with central galaxies from the **redMaPPer** SDSS DR8 (Rykoff et al. 2014) catalog using a $2.0''$ matching radius. Matched objects with a red-sequence photo- z ($0.3 \leq z_{\lambda} < 0.5$) are included in our sample. The accuracy of the red-sequence photo- z is sufficient (median $|z_{\lambda} - z_{\text{Spec}}| \sim 0.01$) for our purpose. The **redMaPPer** catalog provides an additional 133 unique redshifts for massive galaxies in our sample.

In total, at $0.3 \leq z \leq 0.5$, our sample consists of 25286 galaxies with reliable redshift information (referred as **hscZ**). The majority of our redshifts comes from the BOSS and SDSS “legacy” LRG samples. The GAMA survey provides

an additional 14% of all spectroscopic redshifts. Although the GAMA survey only covers parts of the S15B data release, hence affects the homogeneity of our sample, it will not affect the results of this work. We will discuss this more in §5.

We choose the redshift range $0.3 \leq z \leq 0.5$ to make sure that: (1) The inner region of massive galaxies can be resolved, and M_{\star} within 10 kpc can be reliably measured; (2) The background noise and cosmological dimming are not major issues so that the μ_{\star} profile can be measured out to > 100 kpc; (3) Redshift evolution in the stellar population properties can be largely ignored. Also at higher redshift, the completeness of the spec- z sample starts to decline. And finally, the over-subtraction of the background level becomes a more serious issue at lower redshifts.

We will now describe our one-dimensional photometric analysis (§3) and our stellar mass estimates (§4). We will then define the final sample in §5.

3 MEASUREMENTS OF 1-D SURFACE BRIGHTNESS PROFILES

The surface brightness profiles of massive ETG are not well modeled by the de Vaucouleurs or single-Sérsic law, especially at the imaging depth of HSC. These models will fail to simultaneously describe the profile in both the inner and the outer regions and also cannot account for any radial variations in ellipticity and position angle. In principle, massive galaxies can still be described by more complex models (e.g. Huang et al. 2013a,b; Oh et al. 2017), but the results are still sensitive to the choice of a particular model (e.g. de Vaucouleurs or Sérsic profile), the number of components, ini-

⁴ each criterion removes less than 8% of the entire sample.

⁵ See: <http://risa.stanford.edu/redmapper/>

tial guesses of parameters, and internal degeneracies among different parameters. Background subtraction uncertainties can also affect the 2-D model fitting method, especially for the massive ETGs that make up our sample.

We therefore perform elliptical isophote fitting using the IRAF `Ellipse` algorithm (Jedrzejewski 1987) to estimate the total luminosities of massive galaxies and to measure their one-dimensional stellar mass surface density profiles (μ_\star). This 1-D method is less affected by the issues mentioned above. Also, we will only study galaxies in the radial range where we are less sensitive to either the PSF or the background subtraction. We ignore the inner ~ 6 kpc, which is twice the size of $1''$ seeing at $z = 0.5$. Using this conservative choice, we can safely ignore the smearing effect of seeing outside this radius. As we will show later, we confirm this by comparing our HSC profiles with observations with higher spatial resolution. As for the impact from background subtraction, we will focus on the profiles within 100 kpc. This is an empirical, but also conservative choice based on the tests we conducted on background-corrected postage-stamps. Once the surrounding objects are appropriately masked out, the extracted 1-D surface brightness profiles rarely see unphysical truncation or fluctuation within 100 kpc, especially for the $\log(M_{\star,100\text{kpc}}/M_\odot) > 11.6$ galaxies. Please see Appendix B for more details on these tests.

We prepare large *i*-band postage-stamps for each galaxy that extend to 750 kpc in radius, along with a bad pixel mask and the PSF model. These postage-stamps include all of the light of the galaxy and are also large enough to evaluate the background level. We choose to use *i*-band images because they trace the stellar mass distributions of massive galaxies at $0.3 \leq z \leq 0.5$ reasonably well (the observed *i*-band corresponds to a rest-frame *g* or *r* band), but also because they have better seeing and much lower background levels than the *z* and *y* band images (although these in principle may be better tracers of μ_\star).

For each cut-out, to overcome the `hscPipe` “over-deblending” issue, we use a customized procedure to detect and aggressively mask out neighbouring objects. Furthermore, `hscPipe` tends to over-subtract the background around bright objects. To improve the background subtraction, we first aggressively mask out all objects (including the central massive galaxy), and derive an empirical background correction using `SExtractor`. These procedures are described in detail in Appendix B. We should point out that we are not using the photometric results from our customized process, but simply rely on them for improved local background model and appropriate object mask.

Then, we run `Ellipse` on the background-corrected, masked cut-outs following the methodology of Li et al. (2011). In short, we first fit each isophote using a free centroid and shape (ellipticity and position angle). We then fix the centroid (using the mean flux-weighted centroid) and estimate the mean ellipticity and position angles of all isophotes. Finally, we extract a 1-D surface brightness profile along the major axis using the mean ellipticity and position angle. We correct these surface brightness profiles for Galactic extinction and cosmological dimming, and integrate them to various radii to get the luminosity within different physical (elliptical) apertures. Fig 2 shows an example of the 1-D surface brightness and ellipticity profile for a massive galaxy at $z \sim 0.2$ and also highlights a few isophotes.

We test our procedure using different mask sizes, different `Ellipse` parameters, and with or without our background correction. Based on these tests, we find that our 1-D surface brightness profiles are reliable up to surface brightness levels of $i \sim 28.5$ mag arcsec $^{-2}$. Beyond that, some of our profiles shows signs of truncation and/or large fluctuations which are due to either the uncertainty in the background subtraction or the unmasked flux from other objects. We choose to limit our study to surface brightness levels up to ~ 28.5 mag arcsec $^{-2}$. This is a conservative choice but already enables us to measure light profiles out to 100 kpc on a galaxy-by-galaxy basis (no stacking). For more technical details of the `Ellipse` procedure, please see Appendix B.

We cannot extract reliable 1-D profiles for a small fraction of massive galaxies because they are heavily masked out for either physical (e.g. late-stage major merger) or nuisance (e.g. nearby foreground galaxy or bright star) reasons. This is an intrinsic limitation of the 1-D method, and it removes $\sim 10\%$ of the sample. We visually examine the 3-color images of randomly selected galaxies with failed 1-D profiles. Most of them are relative small galaxies that are severely contaminated by nearby objects, and will not affect the results of this work. Meanwhile, it is worth noting that this does exclude most major merging systems among massive galaxies.

Given exquisite profiles extending to 100 kpc, the definition and meaning of “total” magnitude (and stellar mass) becomes nuanced. With the help of the average M_\star/L_\star estimated in the next section (§4), we integrate the profile to a range of radii, and estimate the stellar mass within these different projected 2-D apertures. Motivated by the two-phase scenario, we will consider two benchmark physical apertures throughout this work:

- **The M_\star within the inner 10 kpc** (hereafter noted $M_{\star,10\text{kpc}}$). According to the two-phase scenario, the *in situ* star-formation phase quickly builds up the inner, dense core of massive ETGs. Based on recent observation (e.g. van Dokkum et al. 2010) and simulations (e.g. Rodriguez-Gomez et al. 2016), the *in situ* component dominates the M_\star within one effective radius (R_e , or 5-10 kpc) of $z \sim 0$ massive ETGs. We therefore use $M_{\star,10\text{kpc}}$ as a proxy for the mass formed during the *in situ* phase. Given the quality of the HSC data, we can reliably measure $M_{\star,10\text{kpc}}$ over our redshift range ($1.0''$ in radius equals 4.4 and 6.1 kpc at redshifts 0.3 and 0.5 respectively). It is worth noting that, at the very high- M_\star end, accreted stars may make a significant contribution to the mass within 10 kpc (e.g. Rodriguez-Gomez et al. 2016). We will further discuss the justification of this assumption in 7.1.

- **The stellar mass within 100 kpc** (hereafter noted $M_{\star,100\text{kpc}}$). For our galaxy sample, a 100 kpc aperture corresponds to $5\text{-}10 \times R_e$. We show in § 4.2 that most of the total M_\star for these ETGs lies within a 100 kpc radius and that $M_{\star,100\text{kpc}}$ is a good proxy for the “total” M_\star . Although not perfect, we argue that our measurements of $M_{\star,100\text{kpc}}$ (which are actually measuring the light directly out to 100 kpc) are a better tracer of total M_\star than model-dependent results from shallower data (such as SDSS) which rely on extrapolating the light profiles of galaxies out to large radii.

We should point out that both $M_{\star,10\text{kpc}}$ and $M_{\star,100\text{kpc}}$ are measured after adopting a isophote with fixed ellipticity

and position angle. The 10 kpc and 100 kpc here refer to the radius along the major axis of the elliptical isophote.

4 STELLAR MASSES AND MASS DENSITY PROFILES

4.1 Stellar Masses from SED Fitting

To convert luminosities into M_\star , we assume that these massive galaxies can be well described by an average M_\star/L_\star . This is a reasonable assumption considering that they are mostly dominated by old stellar populations and are known to have only shallow color gradients. We will further justify this point by measuring their median color profiles in § 6.3.

We use the broadband Spectral Energy Distributions (SEDs) fitting (see Walcher et al. 2011 for a recent review) code *iSEDFit*⁶ (Moustakas et al. 2013) to estimate the average M_\star/L_\star and k -corrections using 5-band HSC *cModel* fluxes. Although *cModel* tends to underestimate the total fluxes of bright, extended objects, it can still yield accurate *average* colors thanks to the forced-photometry method that takes the PSF convolution into account (e.g. Huang et al. 2017).

iSEDFit takes a simplified Bayesian approach. In short, it first generates a large grid of SEDs from synthetic stellar population models by drawing randomly from the prior distributions of relevant parameters (e.g. age, metallicity, dust extinction, and star formation history). Based on these models, it uses the observed photometry and redshift to compute the statistical likelihood, and generates the posterior probability distribution functions (PDF) for each parameter. To get the best estimate of a given parameter, *iSEDFit* integrates the full PDF over all the other nuisance parameters. Then, the median value and the $1\text{-}\sigma$ uncertainty are derived based on the marginalized PDF. Please refer to Moustakas et al. (2013) for technical details.

In this work, we derive average M_\star/L_\star using the Flexible Stellar Population Synthesis⁷ (FSPS; v2.4; Conroy & Gunn 2010a, Conroy & Gunn 2010b) model based on the MILES⁸ (Sánchez-Blázquez et al. 2006, Falcón-Barroso et al. 2011) stellar library and assuming a Chabrier (2003) IMF between 0.1 to $100 M_\odot$. The star formation history (SFH) is assumed to follow a delayed- τ model with stochastic star bursts (see Appendix C). This SFH is appropriate for massive galaxies at low redshifts (e.g. Kauffmann et al. 2003). For stellar metallicity ($[M/H] = \log(Z/Z_\odot)$), we assume a flat distribution between 0.004 to 0.03 (the highest value allowed by FSPS). We adopt the Calzetti et al. (2000) extinction law with a order two Gamma distribution of A_V between 0 to 2 magnitudes. The majority of our galaxies are red and quiescent so the results are not very sensitive to parameters related to the SFH or the internal dust extinction. To achieve reasonable sampling across these parameters, we generate 250000 models.

We construct five-band SEDs using the forced-photometry *cModel* magnitudes corrected for Galactic extinction. Presently, *cModel* only accounts for the statisti-

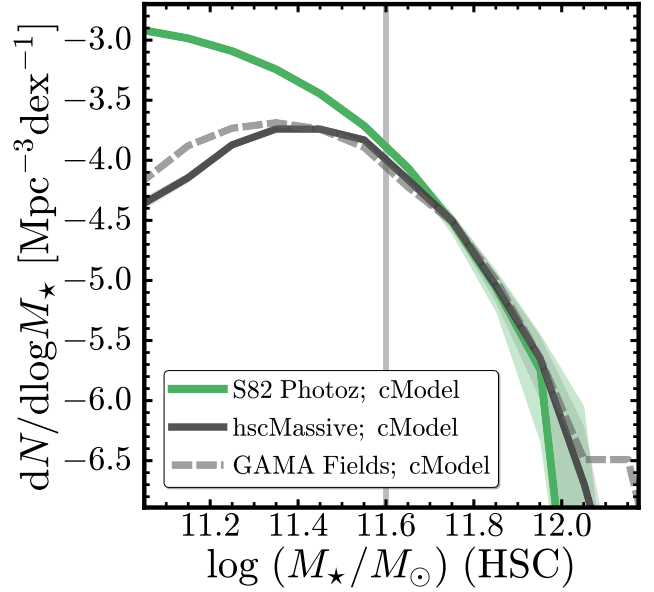


Figure 4. Evaluation of the M_\star completeness of the HSC massive galaxy sample. We compare the volume number density function of the massive galaxies for this work (black line) with the one of a much more complete sample from the S82-MGC catalog (green line). The grey dashed line shows the number density function of HSC massive galaxies in the three GAMA fields for comparison. The associated uncertainties derived from bootstrap resampling are shown in shaded regions. The vertical grey line highlight the $\log(M_\star/M_\odot) = 11.6$ limit. Below it, the HSC massive galaxy sample becomes significantly incomplete in stellar mass.

cal error on the flux measurement and it certainly underestimates the true flux errors of bright galaxies. For this work, we supply *iSEDFit* with simplified flux errors assuming $S/N = 100$ for the *riz* bands, and $S/N = 80$ for the *g* and *y* band (on average, images in *gy* bands are shallower in depth and/or have higher background noise). These empirical S/N choices still only provide lower-limits of the true systematic uncertainties from the model-fitting process. In Huang et al. 2017, we evaluate the accuracy of HSC *cModel* photometry using synthetic galaxies, and show that *cModel* provides excellent measurements of five-band colors, which are crucial for reliable M_\star/L_\star estimates. The typical uncertainty of $\log(M_\star/M_\odot)$ is around 0.06-0.08 dex at $\log(M_\star/M_\odot) \sim 11.5$.

In Appendix C, we briefly summarize the basic statistics of the sample by showing the relationships between $M_\star, 100\text{kpc}$ and stellar age, metallicity, and internal dust extinction. All these properties behave reasonably for massive galaxies in this sample. Using the k -corrected optical color, we can also confirm that the sample follows a tight “red-sequence”. Please see Appendix C for further details.

4.2 “Total” Stellar Masses

Using the best-fit M_\star from *iSEDFit* (noted as $M_{\star, \text{cModel}}$), we estimate the average M_\star/L_\star in the *i*-band, then use that M_\star/L_\star to convert our 1-D luminosity density profiles into stellar mass density (μ_\star) profiles. We also convert our 10 and 100 kpc aperture luminosities into corresponding stellar mass estimates (noted as $M_{\star, 10\text{kpc}}$ and $M_{\star, 100\text{kpc}}$).

⁶ <http://www.sos.siena.edu/~jmoustakas/isedfit/>

⁷ <http://scholar.harvard.edu/cconroy/sps-models>

⁸ <http://www.iac.es/proyecto/miles/pages/stellar-libraries>

For the remainder of this paper, we will use $M_{\star,100\text{kpc}}$ as a proxy of “total” stellar mass. As expected, the integration of the 1-D profile out to very large radius recovers more luminosity (stellar mass) compared to the `cModel`-based estimates (Fig 3). At the high- M_{\star} end (e.g. $\log(M_{\star,100\text{kpc}}/M_{\odot}) > 11.6$), the average difference is larger than 0.1 dex and can be as large as 0.2–0.3 dex. More importantly, the differences between $M_{\star,100\text{kpc}}$ and $M_{\star,\text{cModel}}$ clearly show a dependence on total stellar mass as $M_{\star,\text{cModel}}$ tends to miss more light in more massive galaxies. This relates to the mass-dependent nature of the stellar halos of massive galaxies and the intrinsic limitation of `cModel` method, which we will discuss more in the next section. Such differences also have important implications for estimates of the stellar mass function and for studies of the environment-dependence of galaxy structure. These topics will be discussed in § 7.

Although 100 kpc is already a very large radius that should enclose the majority of stars that belong to these massive galaxies, we know that their μ_{\star} profiles extend beyond 100 kpc without showing any signs of truncation (e.g. Gonzalez et al. 2005; Tal & van Dokkum 2011; D’Souza et al. 2014). Therefore, for massive galaxies, even $M_{\star,100\text{kpc}}$ should be only considered a lower limit on the “total” M_{\star} . In Fig 3, we integrate the μ_{\star} of each galaxy to the edge of the postage-stamp, and pick the isophote that gives us the highest luminosity to estimate the M_{\star} within and call this one $M_{\star,\text{Max}}$. The right panel of Fig 3 compares $M_{\star,\text{Max}}$ and $M_{\star,100\text{kpc}}$. Uncertainties in the background subtraction, and the impact of neighbouring objects, means that $M_{\star,\text{Max}}$ is much more uncertain than $M_{\star,100\text{kpc}}$. Nonetheless, we do see that $M_{\star,\text{Max}}$ is larger than than $M_{\star,100\text{kpc}}$. However, the mass differences are on average very small ($\sim 0.02 - 0.03$ dex) and do not show a strong mass dependence. This confirms that, at the current depth of HSC images, $M_{\star,100\text{kpc}}$ can be used as a good proxy of “total” stellar mass.

Our methodology ignores radial variations in M_{\star}/L_{\star} . It is well known that massive ETGs have negative optical color gradients indicating gradients in M_{\star}/L_{\star} (e.g. Carollo et al. 1993; Davies et al. 1993; La Barbera et al. 2012; D’Souza et al. 2015). Assuming all massive galaxies in our sample have negative color gradients, and there is a simple monotonic relation between optical color and M_{\star}/L_{\star} , the average M_{\star}/L_{\star} we used should in principle underestimate the M_{\star} in the center while overestimate the M_{\star} in the outskirts. However, these color gradients are shallow and smooth out to a few times the effective radius (e.g. La Barbera et al. 2010; Tal & van Dokkum 2011; D’Souza et al. 2014, color gradients at larger radii are not yet well quantified). Because the gradients are shallow, using an average M_{\star}/L_{\star} is unlikely to bias our results on M_{\star} measurements. In Huang et al. (2016b), the authors conduct multi-band decomposition for a sample of very nearby elliptical galaxies, and estimate the M_{\star}/L_{\star} of each component separately. The sum of all components suggest a slightly higher M_{\star} (0.05 – 0.10 dex when typical uncertainty of M_{\star} is 0.12–0.15 dex) and the mass differences show no dependence on M_{\star} .

Color gradients will be discussed more in § 6.3. In summary, our results about the mass dependence of μ_{\star} profiles should not be affected by the assumption of a constant M_{\star}/L_{\star} ratio because optical color gradients in our sample do not show a dependence on stellar mass.

4.3 Stellar Mass Completeness

With the help of the Stripe82 Massive Galaxy Catalog (S82-MGC, Bundy et al. 2015)⁹, we investigate the M_{\star} completeness of our samples. The S82-MGC sample matches the deeper SDSS photometric data in the Stripe 82 region (Annis et al. 2014) with the near infrared data from the United Kingdom Infrared Telescope Infrared Deep Sky Survey (UKIDSS; Lawrence et al. 2007). Comparing to normal SDSS images, the deeper photometry and better photo-zs from S82-MGC make this sample complete to $\log(M_{\star}/M_{\odot}) \geq 11.2$ at $z < 0.7$ which makes it sufficient to evaluate the completeness of our HSC sample. By comparing with the S82-MGC sample (Bundy et al. 2015), Leauthaud et al. (2016) have measured the M_{\star} completeness of the combined BOSS and SDSS samples. They estimate that the BOSS spec-z sample, which is the main source of redshifts for our sample, is about 80% complete at $\log(M_{\star}/M_{\odot}) \geq 11.6$ at $0.3 < z < 0.5$. The GAMA survey is 80% complete down to $10^{10.8} M_{\odot}$ at $z \sim 0.3$, but is only 80% complete to $10^{12.0} M_{\odot}$ at $z \sim 0.5$ according to Taylor et al. (2011) (e.g. their Fig. 6).

There are 20453 S82-MGC galaxies that are also in the `hscPho` sample at $0.3 \leq z_{\text{S82}} \leq 0.5$. Because the S82-MGC uses `cModel` magnitudes, in this section we use $M_{\star,\text{cModel}}$ for consistency with the S82-MGC catalog. The S82-MGC also uses `iSEDFit` with similar assumptions as used in this work and we find excellent agreement between HSC $M_{\star,\text{cModel}}$ and the mass derived by S82-MGC which includes NIR data from UKIDSS.

Figure 4 compares the number density distributions of galaxies from S82-MGC with those from our sample¹⁰. Based on Fig. 4, we conclude that our sample of massive galaxies is reasonably complete down to $\log(M_{\star,\text{cModel}}/M_{\odot}) \sim 11.5$ at $0.3 \leq z \leq 0.5$. Given the average difference between $M_{\star,100\text{kpc}}$ and $M_{\star,\text{cModel}}$, we will focus on galaxies with $\log(M_{\star,100\text{kpc}}/M_{\odot}) > 11.6$ where our sample shows good completeness. In our discussion section, we will also show results for massive galaxies with $11.4 \leq \log(M_{\star,100\text{kpc}}/M_{\odot}) < 11.6$ but we caution that our sample is incomplete in this lower mass bin mainly due to the intrinsic incompleteness of the SDSS/BOSS spec-z (see Leauthaud et al. 2016).

5 THE FINAL SAMPLE

With M_{\star} estimates in hand, we now use the `redMaPPer` galaxy cluster catalog to create a sample of massive central galaxies. The “central” galaxy is defined as the galaxy that lives in the center of its own dark matter halo. In contrast, a galaxy in a sub-halo that is orbiting within the virial radius of a more massive halo is referred to as a “satellite”. To better understand the connection between the structures of massive galaxies and the assembly history of both their stars and dark matter halos, we wish to focus on central galaxies in this work.

⁹ <http://www.ucolick.org/~kbundy/massivegalaxies/s82-mgc.html>

¹⁰ We do not apply any statistical corrections for completeness and hence we do not use the term “stellar mass function” to avoid confusion; Errors on the distributions are estimated via bootstrap resampling.

5.1 Candidate massive central galaxies

Although the central galaxies of dark matter halos have unique importance in studying galaxy-halo connection, robust identification of central galaxy is not easy (e.g. Yang et al. 2007) in observation. First, based on previous results (Reid et al. 2014; Hoshino et al. 2015; Saito et al. 2016), the satellite fraction at $\log(M_{\star,100\text{kpc}}/M_{\odot}) > 11.6$ should be quite low ($\sim 10\%$ level). And, we can further use the redMaPPer catalog to identify and exclude massive satellites in cluster-level dark matter halos—to further reduce contamination from satellite galaxies.

We use v5.10 of the redMaPPer cluster catalog (e.g. Rykoff et al. 2014; Rozo et al. 2015b). These authors have developed a well-tested red-sequence cluster finder that has been run on SDSS DR8 (Aihara et al. 2011) images. For each cluster, the catalog provides a photometric redshift (z_{λ}), a cluster richness (λ), and identifies the most likely central galaxy (the galaxy with the highest P_{Cen} value). The redMaPPer catalog also provides a list of member galaxies for each cluster and their associated membership probabilities. Details about the performance of the redMaPPer cluster catalog can be found in Rozo & Rykoff (2014), Rozo et al. (2015a), and Rozo et al. (2015b).

Several studies have published calibrations between the redMaPPer richness estimate, λ , and halo mass (e.g. Saro et al. 2015; Farahi et al. 2016; Simet et al. 2016; Melchior et al. 2016). All these studies consistently find that redMaPPer clusters with $\lambda > 20$ generally have $\log(M_{\text{halo}}/M_{\odot}) \geq 14.0$, although the scatter of $M_{200\text{b}}$ at fixed λ cannot be ignored. Therefore the central galaxies of these redMaPPer clusters¹¹ form a sample of massive central galaxies that live in massive halos as described above. Such information is also very useful in studying the relationship between galaxy structure and environment (Huang et al. in prep.).

After matching the hscZ sample with the central galaxies of redMaPPer clusters with $\lambda \geq 20$ and $P_{\text{Cen}} \geq 0.7$, we find 164 matched galaxies at $0.3 \leq z \leq 0.5$. This sample of **central galaxies in more massive halos** will be referred to as the **cenHighMh** sample. It is also worth pointing out that, due to the depth and resolution of SDSS images, this redMaPPer catalog is not complete down to $\lambda = 20$ at $0.3 < z < 0.5$. At $z \geq 0.33$, it starts to miss a small fraction of clusters with $\lambda < 30$, but the main results of this work will not be affected by this.

As a next step, we want to construct a sample of central galaxies living in halos with $\log(M_{200\text{b}}/M_{\odot}) < 14.0$. To achieve this, we identify and remove all galaxies within a cylindrical region around all redMaPPer clusters. We use a radius equal to $R_{200\text{b}}$ and the length of the cylinder is set to twice the value of the photometric redshift uncertainty of each cluster.

We convert λ of each cluster to $M_{200\text{b}}$ using the calibration of Simet et al. (2016) and we use the mass-concentration relation from Diemer & Kravtsov (2015) to compute $R_{200\text{b}}$. At $0.3 < z < 0.5$, the uncertainty of photo- z is between 0.015 to 0.025, and is enough to exclude cluster members.

After removing galaxies associated with redMaPPer clusters, the remaining galaxies in our sample will be dominated by central galaxies living in halos with $\log(M_{200\text{b}}/M_{\odot}) < 14.0$.

We will refer to this sample of **galaxies in less massive halos** as the **cenLowMh** sample. Because we have rejected satellites in redMaPPer clusters, and because above our galaxy mass cut most satellites reside in halos with $\log(M_{200\text{b}}/M_{\odot}) > 14.0$ (e.g. Reid et al. 2014; Hoshino et al. 2015; Saito et al. 2016; van Uitert et al. 2016), galaxies in the **cenLowMh** sample should be dominated by central galaxies. Using the model presented in Saito et al. (2016), we estimate that in dark matter halos with $\log(M_{200\text{b}}/M_{\odot}) < 11.4$, $\sim 7\%$ of galaxies with $\log(M_{\star,\text{cModel}}/M_{\odot}) > 11.5$ are satellites. This confirms that our sample should have low enough satellite contamination so that it can be taken as representative massive central galaxies.

5.2 Summary of Sample Construction

Using $\sim 100 \text{ deg}^2$ of HSC data, we select a large sample of massive central galaxies with reliable redshift information, and broadly separate them into two categories based on M_{halo} .

The following is a summary of our sample construction.

- **hscPho** sample: this parent sample consists of bright galaxies with $i_{\text{cModel}} \leq 21.0$, good quality imaging, and reliable **cModel** photometry in all five HSC bands in the **S15B** data release. This sample is described in §2.3, and it contains 1760845 galaxies.

- **hscZ** sample: we limit the **hscPho** sample to galaxies with reliable redshift information. More details of this sample can also be found in §2.3. It provides us 25286 useful galaxies at $0.3 < z < 0.5$.

- With the help of the redMaPPer cluster catalog, we further select candidates of massive central galaxies. We broadly divide the sample into central galaxies living in halos with $\log(M_{200\text{b}}/M_{\odot}) \geq 14.0$ (**cenHighMh**) and $\log(M_{200\text{b}}/M_{\odot}) < 14.0$ (**cenLowMh**). To ensure the sample is M_{\star} -complete and has minimal satellite contamination, we will further focus on the 950 massive galaxies with $\log(M_{\star,100\text{kpc}}/M_{\odot}) > 11.6$ in this work¹².

The division of our sample into two halo mass bins is mainly relevant for Paper II (Huang et al. in prep.). For the present paper, we only consider the halo mass dependence on our sample when we evaluate impact of mass estimates on the SMF in §6.1. We show the distributions of redshift, $M_{\star,100\text{kpc}}$ and $M_{\star,10\text{kpc}}$ of the massive galaxy sample in Appendix A, along with its $M_{\star,100\text{kpc}}-(g-r)$ rest-frame color relation.

6 RESULTS

6.1 Impact of Missing Light on the Galaxy Stellar Mass Function

The Stellar Mass Function (SMF) and its evolution are critical to our understanding of galaxy evolution. On average, the integration of our carefully derived non-parametric μ_{\star} profiles to 100 kpc ($M_{\star,100\text{kpc}}$) recovers more light (hence mass) than the **cModel** method. At $\log(M_{\star,100\text{kpc}}/M_{\odot}) > 11.6$,

¹¹ We only use central galaxies with $P_{\text{CEN}} \geq 0.7$

¹² As reference, there are 2613 massive galaxies with $\log(M_{\star,100\text{kpc}}/M_{\odot}) > 11.5$ in our sample.

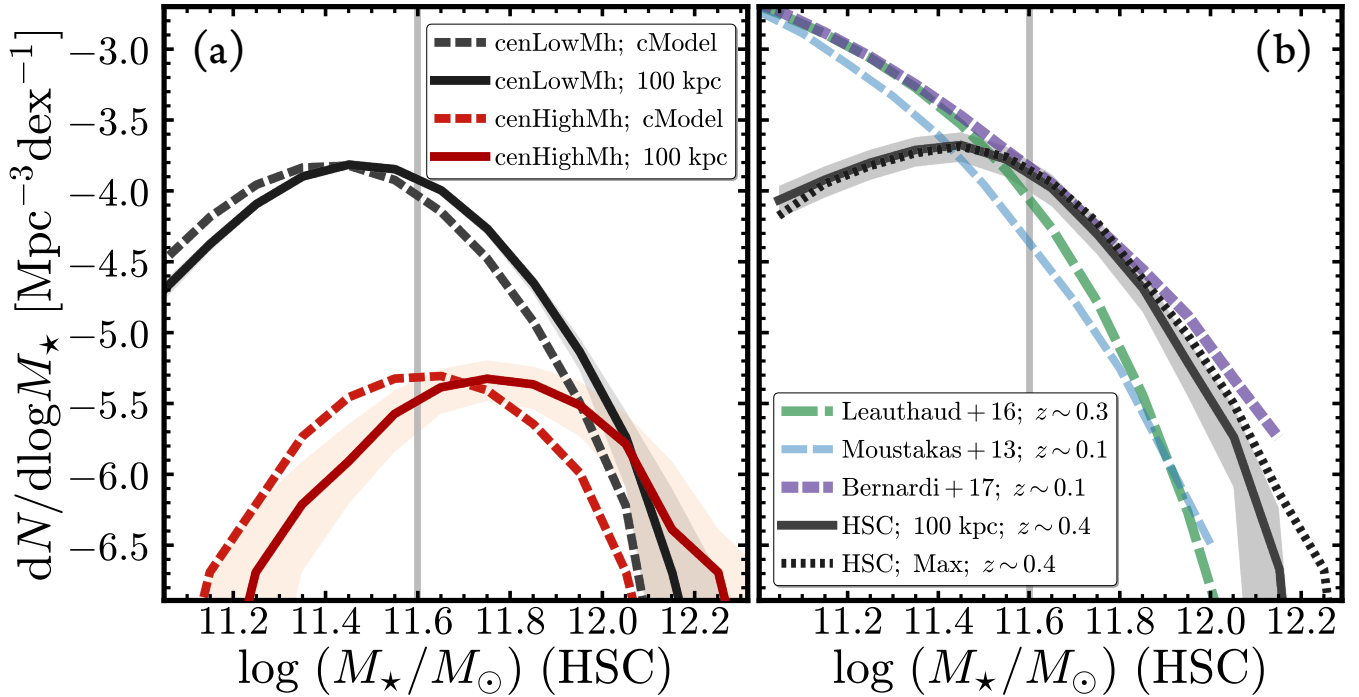


Figure 5. **Left:** Impact of using $M_{\star,100kpc}$ on the galaxy stellar mass function. Dashed lines correspond to the observed volume density distribution computed using $M_{\star,cModel}$ whereas solid lines correspond to the distribution computed using $M_{\star,100kpc}$. We do not apply any completeness correction to the distributions here. Here we separate our HSC sample into centrals in halos more massive than $\log(M_{200b}/M_\odot) \sim 14.2$ (red lines) and centrals in halos with $\log(M_{200b}/M_\odot) < 14.0$ (black lines). The impact on the SMF can exceed 0.2 dex for massive central galaxies in very massive halos. **Right:** The M_\star volume density distributions of massive HSC galaxies, using both $M_{\star,100kpc}$ (black solid line) and $M_{\star,Max}$ (black dotted line). Vertical lines on both plots highlight the $\log(M_{\star,100kpc}/M_\odot) = 11.6$ mass limit. The grey shaded region shows the resampling error on the HSC SMF plus an additional 20% uncertainty to account for the fact that we do not include satellite galaxies and that we fail to extract a 1-D profile for $\sim 10\%$ of our galaxies. These issues will be addressed in forthcoming work. We compare our results with previous studies: (a): SDSS galaxies at $z \sim 0.1$ from Bernardi et al. (2017) with M_\star values based on photometry from 2-D Sérsic + Exponential model fitting (purple); (b): SDSS galaxies at $z \sim 0.1$ from Moustakas et al. (2013) based on improved SDSS cModel photometry (blue); (c): S82-MGC galaxies at $0.15 < z < 0.43$ from Leauthaud et al. (2016) based on PSF-matched SDSS-UKIDSS photometry (green).

the difference can sometimes be larger than 0.2 dex. More importantly, the average difference steadily increases with $M_{\star,100kpc}$. These differences relate to the intrinsic limitation of the cModel method and also reflect the fact that more massive ETGs tend to have more extended stellar mass distributions (e.g. higher-Sérsic index, Graham & Guzmán 2003). Hence, the determination of the “total luminosities” of massive galaxies can result in a significant impact on the high mass end of the galaxy stellar mass function (e.g. Bernardi et al. 2013; D’Souza et al. 2014, 2015; Bernardi et al. 2017).

In this paper, we have only measured light profiles for central galaxies. Also, we cannot extract 1-D profiles for $\sim 11\%$ of galaxies (because contamination from nearby bright object is too severe; or the its in a late-stage on-going merger system). These two effects will lead to a $\sim 20\%$ uncertainty in the amplitude of our volume number density distributions. Both of these effects show dependence on $M_{\star,100kpc}$ whereas more massive galaxies suffer slightly less from them. We are currently working to address these limitations in a forthcoming paper. Our goal in this paper is therefore not to attempt a detailed comparison between different SMFs (e.g., Bernardi et al. 2013, 2017). Instead, our goal in this

section is simply to characterize the impact of various M_\star measurements on the high-mass end of the SMF. Our volume density distributions (will be referred to as SMF for simplicity) turn over at the low-mass end where the sample becomes incomplete, and we do not attempt to apply any completeness correction here.

Figure 5 displays the impact of missing light and of different definitions of M_\star on the SMF. The left panel of Fig. 5 shows the SMF computed using $M_{\star,cModel}$ and $M_{\star,100kpc}$ for galaxies that live in low and high mass halos. Figure 5 shows that the impact of missing flux is more severe for galaxies in high mass halos. In Paper II of this series (Huang et al. in prep.), it will be demonstrated that this occurs because galaxies in more massive halos have more extended stellar envelopes than those in lower mass halos at fixed $M_{\star,100kpc}$. Figure 5 also shows that the use of the HSC cModel magnitude leads to a severe underestimation of M_\star at the high mass end of SMF. From the current hscPipe, this problem could relate to the intrinsic limitation of simply model like cModel and the issue of over-subtracted background. Based on the 1-D surface brightness profiles in i -band, background subtraction does not seem to be the most serious problem for these $z > 0.3$ galaxies (at least not within 100 kpc). And,

in the next section, we will show that a significant fraction of these 1-D profiles are more extended in the outskirts than the de Vaucouleurs profile, therefore it is not surprising that `cModel` will systematically underestimate their total flux.

As discussed in § 4.2, even with deep HSC images, it is not trivial to clearly define and measure the “total” M_\star for these massive systems, and the μ_\star profiles of these galaxies often extend well beyond 100 kpc. Is our fiducial 100 kpc radius sufficient to capture most of the flux associated with these galaxies, or does one need to integrate out to even larger radii? To answer this question, we attempt to capture more flux by integrating our μ_\star profiles out to the edge of the image and use the highest M_\star achieved during this process as $M_{\star, \text{Max}}$. Although the μ_\star profiles become more uncertain at > 100 kpc, $M_{\star, \text{Max}}$ helps us quantify how much extra M_\star may be contained at radii greater than 100 kpc. The right hand side of Figure 5 shows the impact of using $M_{\star, \text{Max}}$ instead of $M_{\star, 100\text{kpc}}$ on the SMF. We find that a 100 kpc radius captures a majority of the galaxy mass and that the impact of going from $M_{\star, 100\text{kpc}}$ to $M_{\star, \text{Max}}$ is relatively small.

In Figure 5 we also compare our results with the following previous studies:

- The SMF for $0.15 < z < 0.30$ galaxies from the S82-MGC sample (Leauthaud et al. 2016) where M_\star is derived using `iSEDfit` on PSF-corrected aperture photometry from S82. They adopt the same IMF, dust model, and star-formation model as we do, but use the BC03 model instead. Based on the test results in Appendix C, we shift this SMF by 0.08 dex to add their data to Figure 5.
- The SMF derived from a SDSS-*GALEX* sample of $z \sim 0.1$ galaxies by Moustakas et al. (2013). Total luminosities in Moustakas et al. (2013) are based on SDSS `cModel` magnitudes. They use a M_\star/L_\star that is derived via SED fitting using `iSEDfit` with similar assumptions as the ones adopted here.
- The observed SMF for $z \sim 0.1$ SDSS galaxies from Bernardi et al. (2017). Total luminosities in Bernardi et al. (2017) are based on 2-D `SerExp` models (Sérsic + Exponential disk model; integrated to infinity) that recover more flux compared to SDSS `cModel` magnitudes (Bernardi et al. 2013; Meert et al. 2015). They use a M_\star/L_\star that is adopted from the SED fitting results in Mendel et al. (2014). This model also uses the FSPS stellar population model (Conroy & Gunn 2010a), assumes a Chabrier (2003) IMF, and considers dust extinction using the Calzetti et al. (2000) extinction law (the “dusty” model).

As mentioned above, our current SMF is subject to an additional 20% uncertainty that will be addressed in forthcoming work. Hence, we do not attempt a detailed comparison with respect to previous works on the SMF, reserving this for a future study. Here, we simply note that the HSC SMF derived using $M_{\star, 100\text{kpc}}$ is close to the one derived by Bernardi et al. (2017) using SDSS data at $z \sim 0.1$ and assuming the `SerExp` models. Our sample and the Bernardi et al. (2017) sample have different redshifts. Without a more in-depth study, we cannot ascertain whether or not the apparent agreement between the HSC SMF and the Bernardi et al. (2017) SMF indicates a global lack of evolution in the galaxy SMF, or that other effects are at play (for example, the difference between $M_{\star, 100\text{kpc}}$ masses and `SerExp` masses)

that have cancelled redshift evolution. In future work, it will be interesting to perform a more consistent analysis to search for redshift evolution in the galaxy SMF and to study whether or not massive galaxies in HSC are well described by `SerExp` models.

6.2 Surface Mass Density Profiles

6.2.1 General Trends and Comparison with Previous Work

Previous work on the structural evolution of massive galaxies has often focused on scaling relations such as the “ M_\star -size” relation. We argue that comparing μ_\star profiles directly captures more information than the M_\star -size relation and has the advantage that it bypasses difficult questions about how to accurately define and measure galaxy “sizes” and “masses”.

Fig. 6 shows the median μ_\star profiles of massive central galaxies at $0.3 < z < 0.5$ in three $M_{\star, 100\text{kpc}}$ bins. These median profiles along with their uncertainties are derived using bootstrap resampling method. Note that our sample is not complete in the lowest $M_{\star, 100\text{kpc}}$ bin, although the median μ_\star profile may not be significantly affected. As shown in the left panel of Fig 6, we can comfortably trace the μ_\star profiles of these massive galaxies out to 100 kpc **individually**. At large scales, some of our μ_\star profiles show signs of unphysical truncation and fluctuation related to inaccurate sky subtraction. In this paper, we do not use profiles beyond 100 kpc, even though the median μ_\star profiles for the two most massive bins behave reasonably out to ~ 200 kpc.

From Figure 6 we can see the galaxies in our sample have homogeneous profiles on small radial scales. The amplitude of μ_\star increases with galaxy mass on 10 kpc scales but the slope of μ_\star remains similar. From previous work on this topic, we already know that the inner regions of massive elliptical galaxies display relatively uniform structural (e.g. μ_\star profile, isophotal shape: e.g. Lauer et al. 2007; Kormendy et al. 2009; Schombert 2015; and kinematic: e.g. Cappellari et al. 2013) properties. However, Figure 6 reveals a significant diversity in the outer envelopes of massive galaxies. Given the S/N of HSC images at these surface brightness levels, the scatter shown in Figure 6 corresponds to **intrinsic scatter in the stellar envelopes of massive galaxies**. Importantly, Figure 6 shows that the global μ_\star profiles of galaxies at these masses are **clearly not self-similar** out to 100 kpc and have outskirts with larger scatter.

In the right-hand side of Fig. 6, we compare our μ_\star profiles with results from previous work. Deep μ_\star profiles of massive galaxies are rarely available. Even in the nearby universe, it is not trivial to map the low surface brightness outskirts of massive galaxies (e.g., Capaccioli et al. 2015; Iodice et al. 2016, 2017; Spavone et al. 2017; Mihos et al. 2017). The number of very massive galaxies is also very limited in the local universe. For example, according to the MASSIVE survey (Ma et al. 2014), there are only ~ 60 -70 massive galaxies with $\log(M_\star/M_\odot) > 11.6$ (based on K-band luminosity) within 108 Mpc.

Most previous studies have focused on surface brightness profiles instead of mass density profiles. Results can also depend on the stacking technique or the model used to extract the profile (e.g., Tal & van Dokkum 2011; D’Souza et al. 2015). Huang et al. (2013a) derived μ_\star profiles for a

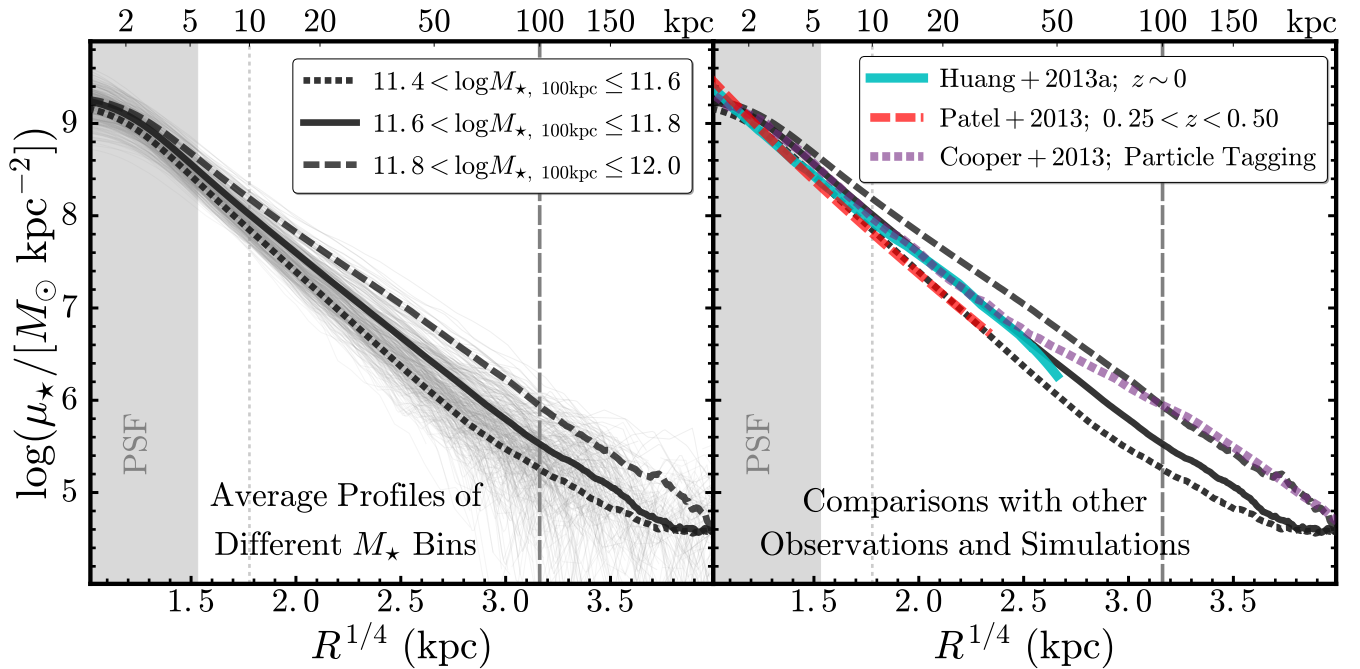


Figure 6. **Left:** Median μ_* profiles in three total stellar mass bins. Thin grey lines show a random subset of individual profiles. The scatter between the thin grey lines reflects the true scatter in the profiles of massive galaxies (not measurement error). The shaded region highlights the region that is most strongly affected by the seeing. Two vertical lines indicate 10 kpc (thin, dotted line) and 100 kpc (thick, dashed line). **Right:** comparison between our μ_* profiles, previous observations, and simulations. The solid cyan line shows the median profile of massive elliptical galaxies at $z \sim 0$ from Huang et al. (2013a). The red long-dashed line shows the median profile of massive galaxies at $0.25 \leq z < 0.50$ observed by *HST* from Patel et al. (2013). The purple short-dashed line shows the median radial stellar distributions in massive halos from simulation using the particle tagging method (Cooper et al. 2013).

small sample of very nearby ellipticals (within 100 Mpc; median $\log(M_*/M_\odot) \sim 11.3$) based on relatively shallow images from the Carnegie-Irvine Galaxy Survey (CGS, Ho et al. 2011)¹³. This sample is at very low redshift ($z < 0.02$), and so the μ_* profiles from Huang et al. (2013a) galaxies are accurate to smaller scales (down to $r = 1$ kpc) than our HSC ones. Our μ_* profiles show good agreement with the Huang et al. (2013a) sample in the radial range of overlap (out to 50 kpc). CGS images are deeper than SDSS images in the r -band, but the median profiles from Huang et al. (2013a) still only reach to ~ 50 kpc for $z < 0.02$ massive galaxies. Meanwhile, our deep HSC images can reliably deliver individual μ_* profiles for $z \sim 0.4$ galaxies out to at least 100 kpc.

Patel et al. (2013) extracted a median μ_* profile for massive ETGs at $0.25 < z < 0.50$ using stacked *HST*/*ACS* images. These galaxies are selected at a constant cumulative number density and are thought to be the progenitors of $z = 0$ massive ETGs (e.g. Leja et al. 2013). The median M_* of the Patel et al. (2013) sample is $\sim 10^{11.2} M_\odot$ which is lower than our lowest mass bin. However, Patel et al. (2013) uses the BC03 stellar population model which leads to M_* that are roughly 0.1 dex lower than our FSPS estimates (see Appendix C). Furthermore, the Patel et al. (2013) images are shallower than ours which means that their M_* could still be underestimated due to missing light in the outskirts. Given these two considerations, it is reasonable to roughly

compare the Patel et al. (2013) profile with the one in our lowest $M_{*,100\text{kpc}}$ bin. The superb resolution of the *HST*/*ACS* images allows Patel et al. (2013) to accurately measure μ_* profile down to 1 kpc without worrying the smearing effect of seeing. The good agreement between our profiles and the ones derived from *HST* imaging demonstrates that our profiles are robust at $r \geq 3$ kpc so that we can accurately measure $M_{*,10\text{kpc}}$.

Finally, we also compare with the predicted median μ_* profile of central galaxies in massive halos ($13.5 < \log M_{200,c} < 14.0$) from a cosmological simulation where the μ_* profiles of galaxies are calculated using the particle-tagging technique (e.g., Cooper et al. 2010). The simulated μ_* profile is affected by the resolution limit of the simulation in the inner region, but is in good agreement with our median μ_* profile for the $11.6 < \log(M_{*,100\text{kpc}}/M_\odot) < 11.8$ bin within 40 kpc. However, outside 40 kpc, the particle tagging method seems to predict a too prominent stellar halo and has much shallower outer slope compared to our data. In future work, we will compare our HSC profiles with predictions from more advanced hydrodynamic simulations such as *Horizon-AGN* (Dubois et al. 2014) and *MassiveBlackII* (Khandai et al. 2015). These data will help fine-tune simulations and to understand the physical mechanisms that drive the assembly of massive galaxies and the build up of stellar halos.

Table 1 provides tabulated values for the median profiles that are displayed in Fig. 6. These profiles are also available

¹³ <https://cgs.obs.carnegiescience.edu/CGS/Home.html>

here. (The files will be made available after the paper is accepted)

6.3 Ellipticity and Color Profiles

So far, we have focused on 1-D μ_\star profiles. We now consider ellipticity and k -corrected optical color profiles. We extract ellipticity profiles using `Ellipse` by leaving the shape of each isophote as a free parameter. We also apply the isophotal information derived in the i -band directly to other filters and extract 1-D $g-r$ and $g-i$ color profiles. We apply the Galactic extinction correction and the `iSEDFit` k -correction to the color profiles. Smearing effect of seeing will make the central isophotal shape rounder than the real value, while seeing differences between filters will bias the central color¹⁴. On large scales, it is more difficult to extract reliable ellipticity and color profiles out to 100 kpc: at low surface brightness levels, the isophotal shape becomes unstable and is easily affected by contamination. Color profiles are also more difficult to extract out to large radial scales because getting the color accurately depends on the background subtraction and the noise levels in both bands. In this paper, we will focus on the median ellipticity and color profiles between 8–60 kpc where we can safely ignore the issues described above.

The ellipticity of the isophotes contains information about the 3-D geometry (e.g. Tremblay & Merritt 1995, 1996; Chang et al. 2013; Rodríguez & Padilla 2013; Mitsuda et al. 2017) and kinematics (e.g. Cappellari et al. 2012; Weijmans et al. 2014) of stars in massive galaxies. The left panel of Fig 7 shows the ellipticity profiles of massive galaxies and highlights the median profiles for the same three $M_{\star,100\text{kpc}}$ bins as used in Fig 6. Our results are also compared with previous work based on image stacking techniques (the PSF-removed i -band results from Tal & van Dokkum 2011, and concentrated galaxies with $11.0 < \log(M_\star/M_\odot) < 11.4$ from D’Souza et al. 2015). As expected, ellipticity profiles from image stacking methods yield results that are more shallow than when ellipticity can be measured on a galaxy-by-galaxy basis. Uncertainties in how to align galaxies, and the intrinsic isophotal twist can lead to this effect.

In general, we find that the ellipticities of massive galaxies slowly increase with radius. This trend can even be seen directly “by eye” in HSC images (e.g. Fig 1). More interestingly, the ellipticity profiles vary with $M_{\star,100\text{kpc}}$: at ~ 10 kpc, the median ellipticity (< 0.2) is similar for all three redshift bins, but the ellipticity of the outer stellar halo increases with $M_{\star,100\text{kpc}}$. Galaxies with $\log(M_{\star,100\text{kpc}}/M_\odot) > 11.8$ have median ellipticity profiles that become steeper at > 10 kpc. The ellipticity of the outer profile steadily increases from $e \leq 0.2$ to $e \sim 0.4$ at 50–60 kpc.

This is consistent with studies of nearby massive galaxies, both from 1-D ellipticity profiles and 2-D modeling results (Porter et al. 1991; Gonzalez et al. 2005; Zibetti et al. 2005; Spavone et al. 2017; Huang et al. 2013a; Oh et al. 2017). However, to the best of our knowledge, our HSC results are the first to show clear evidence that: a) the ellipticity of stellar halo in massive ETGs depends strongly on $M_{\star,100\text{kpc}}$, and b) the ellipticity of stellar halo also relates

to the slope of the μ_\star profile (see Fig 6 and Fig 7; we will discuss this more in Paper II).

If accreted stars dominate the stellar halos of massive galaxies, this mass-dependent ellipticity profile may contain clues about the assembly history of massive galaxies (e.g. average time since last merger, average merger mass ratio). Previous simulations often focused on reproducing the rounder average shape and slow-rotating nature of massive ETGs (e.g. Wu et al. 2014), and the projected ellipticity profiles and their correlations with the kinematic of stars and merging history have not been carefully explored.

Regarding the color profiles, it is well known that massive elliptical galaxies have shallow and negative color gradients that reflect radial variations in their stellar populations (e.g. Carollo et al. 1993; La Barbera et al. 2012) and hence contain information about the assembly history of their stellar halos (e.g. Hirschmann et al. 2015). The right panels of Fig 7 show the k -corrected $(g-r)$ and $(g-i)$ color profiles for all galaxies in our sample, together with the median profiles in three $M_{\star,100\text{kpc}}$ bins. We find the the median rest-frame $(g-r)$ and $(g-i)$ color decreases at larger radii, but there does not appear to be a significant M_\star dependence in the gradient of rest-frame optical colors. We also compare our results with the stacked color profiles from La Barbera et al. 2010¹⁵ and D’Souza et al. 2014. The median color profiles from HSC images are systematically steeper than the stacked SDSS ones. Considering differences in the response curves between HSC and SDSS filters, together with the uncertainties of color measurements, the HSC $(g-r)$ color profiles are in fairly good agreement with those from SDSS. However, the $(g-i)$ profiles of HSC galaxies are steeper compared to SDSS. The SDSS i -band suffers from the so-called “red-halo” effect (e.g. Wu et al. 2005, Tal & van Dokkum 2011). This is due to the fact that the SDSS i -band PSF has more prominent wing than other bands. Because the PSF model does not capture these wings, this artificially distributes more flux to the outskirts, and leads to apparently redder colors in the low surface brightness outskirts of galaxies. Because HSC uses thick CCDs, HSC i -band images do not suffer from this effect and can be used to determine galaxy colors with higher accuracy.

Fairly steep color profiles have been observed in several very nearby massive ETGs. Fig 7 shows the $g-r$ color profiles of NGC 4472 (Mihos et al. 2013) and NGC 4365 (Mihos et al. 2017)¹⁶, and the $g-i$ profile of NGC 1399 (Iodice et al. 2016). These individual profiles display similar color gradients as our HSC sample.

7 DISCUSSION

In this paper, we have used data from the HSC survey that is both simultaneously deep and wide to trace the stellar mass distributions of $0.3 < z < 0.5$ massive galaxies out to > 100 kpc and to reveal the mass-dependent nature of their stellar halos. Here we briefly discuss the scientific implications of our results.

¹⁵ We use the median color profiles of high-mass ETGs; the original profile is in units of R_e , we use a typical $R_e = 8.0$ kpc to convert it into physical kpc.

¹⁶ Both are converted from $(B-V)$ colors.

¹⁴ Since the HSC i -band always has better seeing, the central color will become redder if seeing effects are not accounted for

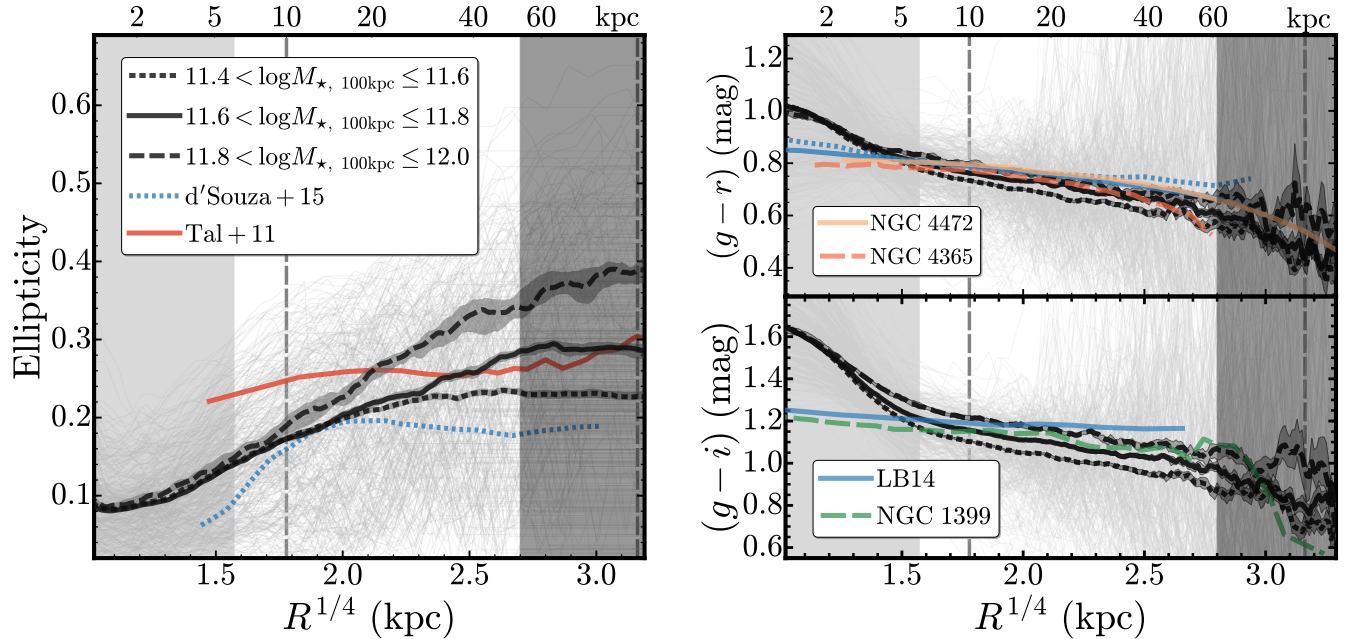


Figure 7. Radial profiles of the ellipticity and k -corrected rest-frame optical colors of massive galaxies in our sample. The general format of this figure is similar to Fig 6. The **left panel** displays ellipticity profiles, the **Upper-right panel** shows $g-r$ color profiles, and the **lower-right panel** is for $g-i$ color profiles. We compare our results with those from (1) [Tal & van Dokkum \(2011\)](#) based on stacking large samples of luminous red galaxies in SDSS at $z \sim 0.4$ (solid red line on the left panel), (2) the results from a stacking analysis of nearby massive galaxies with high concentration index ($C > 2.6$) in [D’Souza et al. \(2014\)](#), (blue dash lines on the left and upper-right panels), (3) and the average $g-r$ and $g-i$ color profiles from a large sample of nearby elliptical galaxies in [La Barbera et al. \(2010\)](#), (blue, solid lines on both right panels). For color profiles, we also compare with deep observations of a few nearby massive ETGs: the $g-r$ color profiles of NGC 4472 ([Mihos et al. 2013](#)) and NGC 4365 ([Mihos et al. 2017](#)), and the $g-i$ profile of NGC 1399 ([Iodice et al. 2016](#)).

7.1 The Formation of Massive Galaxies and the Assembly of Their Outer Halos

We find that the outer halos of massive elliptical galaxies grow more prominent and more elliptical with increasing stellar mass. According to the two-phase formation scenario, the inner 5–10 kpc of these massive central galaxies are formed at $z > 1$ during an intense period of *in situ* star formation. The outskirts of massive galaxies are then built up through a more gradual second phase of evolution (the *ex situ* phase) that is dominated by mass assembly via accretions. Non-dissipative mergers, especially minor mergers¹⁷, mostly deposit stars in the outskirts of centrals and do not have a large impact on the central μ_* profile (e.g. [Boylan-Kolchin et al. 2008](#); [Oogi & Habe 2013](#); [Bédorf & Portegies Zwart 2013](#)). Given the stochastic nature of the merging process, it is easy to understand why the μ_* profiles of massive galaxies are similar in the inner region but show a large scatter in the outer region.

State of the art hydrodynamic simulations of massive galaxy formation predict that the fraction of accreted stars should strongly increase with stellar mass and that for very massive galaxies, the *ex-situ* may reach up to 50-90% of the total galaxy mass (e.g. [Oser et al. 2010](#); [Cooper et al. 2013](#); [Dubois et al. 2013](#); [Lee & Yi 2013](#); [Hirschmann et al. 2015](#); [Rodríguez-Gomez et al. 2016](#)).

This picture is supported by our observations that massive galaxies display more prominent stellar halos as well as by their negative color gradients. The fact that the outskirts of these galaxies are slightly bluer than the inner regions, is consistent with the picture that stellar halos are built up by series of minor mergers (average merger mass-ratio between 1:3-1:10; e.g. [Huang et al. 2016b](#)) as less massive ETGs are typically bluer.

Also according to this picture, the shape of the stellar halo should preserve information about the merging history and possibly even about the shape of the dark matter halo. Simulations show the shape of the stellar and dark matter halos are closely correlated (e.g. [Wu et al. 2014](#)) for slowly-rotating massive ETGs having undergone multiple minor-mergers. The more elongated outer halo and the trend between the ellipticity profile and stellar mass may reflect the orbital properties of accreted satellite. In simulations, satellite orbits become more radial for more massive halos (e.g. [Murante et al. 2007](#); [Wetzel 2011](#); [Jiang et al. 2015](#)). Satellites infalling along radial orbits may help to form elongated stellar halos. In principle, these results may explain the trend that we see. However, in contrast, simulation from [Wu et al. \(2014\)](#) predict that more massive galaxies should have *rounder* outskirts which is the opposite trend compared to HSC. This difference warrants further investigation.

At larger scales, the distribution of satellite galaxies in massive halos is found to be aligned with the major axis of the central galaxy (e.g. [Brainerd 2005](#); [Yang et al. 2006](#); [Niederste-Ostholt et al. 2010](#); [Huang et al. 2016a](#)). This

¹⁷ Normally minor merger means the one with stellar mass ratio smaller than 1:3 or 1:4

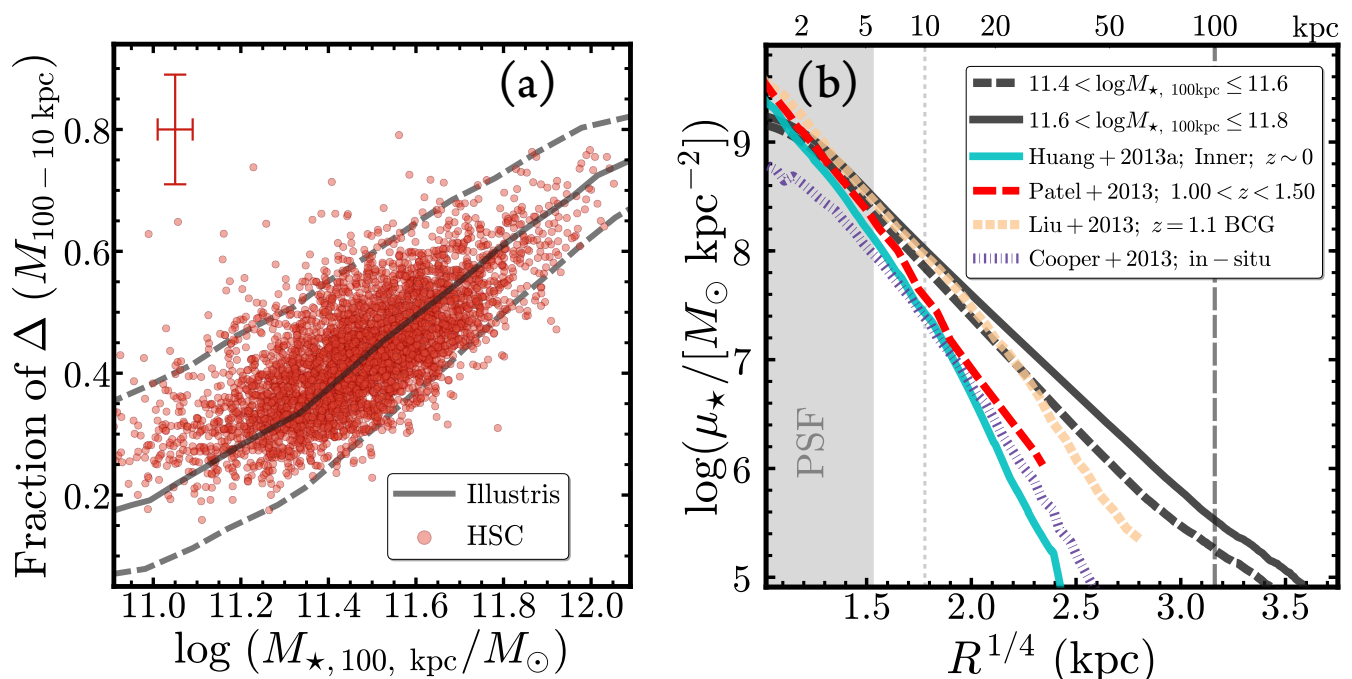


Figure 8. **Left:** Ratio of the fraction of stars between 10 to 100 kpc to the total galaxy mass $M_{\star, 100\text{kpc}}$. We adopt this ratio as a proxy for the fraction of ex-situ stars in our sample. Typical observational uncertainties are shown in the upper left hand corner. The solid grey line shows the predicted relation derived from the Illustris simulation at $z = 0$ (Fig 4 in [Rodríguez-Gomez et al. 2016](#)). Regions between the grey dashed lines correspond to the range between the 16 and 84 percentile of the distribution. **Right:** comparison between our median μ_{\star} profiles with the inner component of the structural decomposition of massive elliptical galaxies at $z < 0.02$ from [Huang et al. \(2013a, Cyan, solid\)](#). At higher redshifts, the μ_{\star} profiles of massive galaxies should be dominated by the in-situ component. We compare our profiles with the median μ_{\star} profile of massive galaxies at $1.0 < z < 1.5$ from *HST* observations [Patel et al. \(2013, Red, dashed\)](#). Both these comparisons suggest that the μ_{\star} profile within 10 kpc is dominated by *in situ* stars, but there are already contributions from the accreted stars at very high M_{\star} end. We also compare with the μ_{\star} profile of a very massive cD galaxy at $z \sim 1.1$ discovered by [Liu et al. \(2013, Yellow, dashed\)](#) in the Hubble Ultra-Deep Field. It is likely that this object will grow into one of the very massive central galaxy in our sample. It is interesting to see that its μ_{\star} profile is very similar to the HSC one of the most massive $M_{\star, 100\text{kpc}}$ bin in the inner ~ 20 kpc, so the following growth should mostly happen in the outskirts.

alignment signal is found to be stronger for more luminous galaxies living in more massive halos (e.g. [Hirata et al. 2007](#)). The fact that more massive central galaxies have steeper ellipticity profiles and become increasingly more elongated in the outskirts may arise because of such alignment. Moreover, the shape of the dark matter halo can be estimated by analyzing satellite distributions and weak lensing profiles ([Clampitt & Jain 2016](#)). It is interesting to point out that the most recent measurement by [Shin et al. \(2017\)](#) around SDSS clusters show a halo axis-ratio of ~ 0.55 , which is only slightly more elongated than the stellar halo of galaxies in our highest $M_{\star, 100\text{kpc}}$ bin.

7.2 Aperture Masses as Proxies of the *In situ* and Accreted Stars

Recent hydrodynamic simulations of galaxy formation often separate stars in galaxies into *in situ* and *ex situ* components. In simulations, the *in situ* component is often defined as the stars formed in the halo of the “main progenitor”. The spatial distribution, kinematic, and stellar population properties of both components are important theoretical predictions. Among various predictions, the fraction of *ex situ* stars and the scaling of the *ex situ* fraction with stellar mass is per-

haps the first aspect to test. However, on the observational side, there is no straightforward way to actually disentangle these two components for massive galaxies. Disk galaxies are more easily decomposed into multiple components and recently, deep surveys of nearby disk galaxies have started to provide constraints on their stellar halos (e.g. [Courteau et al. 2011; Merritt et al. 2016; Harmsen et al. 2017](#))¹⁸.

For more massive ETGs, results so far mainly depend on multi-component model fitting and image stacking analyses (e.g. [Huang et al. 2013a; D’Souza et al. 2014; Spavone et al. 2017](#)). In this work, we propose that M_{\star} computed within different fixed physical apertures are worth exploring as proxies of the *ex situ* fraction. We propose to use the mass within 10 kpc ($M_{\star, 10\text{kpc}}$) and 100 kpc ($M_{\star, 100\text{kpc}}$) as proxies for the *in situ* component and for the total M_{\star} .

On the left panel of Fig 8 we show the relation between $M_{\star, 100\text{kpc}}$ and the fraction of mass between 10 and 100 kpc (as a proxy of the mass of the accreted component). We compare this with the fraction of *ex situ* stars predicted by the Illustris simulation ([Rodríguez-Gomez et al. 2016](#)). We find that our proxy for the accreted mass component cor-

¹⁸ Although it is still not certain that all stellar halos around disk galaxies are made out of *ex situ* stars.

relates strongly with $M_{\star,100\text{kpc}}$ and that this relation is surprisingly consistent with predictions from [Rodríguez-Gomez et al. \(2016\)](#). Given the limitations of the Illustris simulation, and the imperfect nature of our *ex situ* fraction proxy, the almost perfect agreement seen in Figure 8 may well be a coincidence. However, it is encouraging to see that our simple proxy for the fraction of *ex situ* stars seems to match both the slope and the scatter of the predicted relation. There exists other hydrodynamic simulations that predict significantly different *ex situ* fractions compared to Illustris (e.g. [Lackner et al. 2012](#); [Qu et al. 2017](#)). In future work, we will explore more detailed comparisons between our data and predictions from hydrodynamic simulations and we will investigate to what degree simple elliptical aperture masses may be used to trace *ex situ* fractions.

How well justified is our choice of $M_{\star,10\text{kpc}}$ as a proxy of the *in-situ* component? A full investigation is beyond the scope of this paper. Here we simply present comparisons between our profiles and a) several estimates of the *in-situ* component and b) observations of high redshift massive galaxies that should be dominated by the *in situ* component. In particular, we compare with:

(i) The median μ_{\star} profiles of massive ETGs at $1.0 < z < 1.5$ from [Patel et al. 2013](#). These are considered to be the progenitors of $\sim 10^{11.5} M_{\odot}$ ETGs at $z = 0$ and their inner region should be dominated by *in situ* stars.

(ii) The inner component of $z \sim 0$ ellipticals from the 2-D decomposition of [Huang et al. \(2013a\)](#). [Huang et al. \(2013b\)](#) show that this inner component is structurally similar to the compact “red nuggets” at high- z .

(iii) The *in situ* components of simulated central galaxies in massive halos from [Cooper et al. \(2013\)](#) (the inner ~ 5 kpc is quite uncertain due to the resolution). These μ_{\star} profiles are generated using the particle tagging method (see [Cooper et al. 2010](#))

We also compare with a uniquely massive BCG at high redshift: a $\log(M_{\star}/M_{\odot}) \sim 10^{11.4} M_{\odot}$ BCG with a distinctive “cD”-like envelope at $z \sim 1.1$ ([Liu et al. 2013](#)). This high redshift galaxy has a μ_{\star} profile that follows the median μ_{\star} profile of our $11.6 \leq \log(M_{\star,100\text{kpc}}/M_{\odot}) < 11.8$ sample nicely at $R < 20$ kpc, but the profile becomes much steeper in the outskirts. This suggests that the inner “core” of massive BCGs are already in place at $z \sim 1$ while the outer halo is still being assembled.

These simple comparisons certainly support the idea that $M_{\star,10\text{kpc}}$ mainly consists of *in situ* stars whereas mass at $R > 15\text{--}20$ kpc is dominated by *ex situ* component. Meanwhile, this comparison also shows that the *in situ* component may extend beyond 10 kpc¹⁹. Further comparisons with massive galaxies at high redshift and with hydrodynamical simulations will help understand which radius is optimal for probing the *in situ* mass.

¹⁹ We convert these μ_{\star} profiles to the same [Chabrier 2003](#) IMF; but there are still differences in median M_{\star} and details in the M_{\star}/L_{\star} estimates

8 SUMMARY AND CONCLUSIONS

In this work, we study how the projected stellar mass density profiles and other structural properties of massive central galaxies depend on their total stellar mass using deep images from the Subaru HSC survey. With the help of this high-quality and wide area data set, we directly map the stellar mass distributions of ~ 7000 massive central galaxies at $0.3 < z < 0.5$ out to > 100 kpc without resorting to stacking techniques. We group massive central galaxies into two categories based on their host halo mass ($M_{200\text{b}} \gtrsim 10^{14.0} M_{\odot}$ and $M_{200\text{b}} \lesssim 10^{14} M_{\odot}$) and three bins of $M_{\star,100\text{kpc}}$. Our main results are:

(i) We find that the “total” M_{\star} of these massive galaxies can be significantly underestimated with shallow imaging data such as SDSS and/or oversimplified model assumptions (e.g. the `cModel` or single-Sérsic). In contrast to previous work, our results do not depend on stacking or any parametric models. Moreover, the degree to which stellar mass is underestimated depends on $M_{\star,100\text{kpc}}$. Simple model misses more light for massive galaxies because they have more extended envelopes. There is also a $M_{200\text{b}}$ -dependence of this effect and naive luminosity estimates will miss more light for BCGs in more massive halos compared to centrals in less massive halos. These effects need to be carefully taken into account when discussing topics such as the evolution of the galaxy stellar mass function.

(ii) We show that the μ_{\star} profiles of massive galaxies are relatively homogenous within 10-20 kpc. However, there is large scatter in outer profiles of massive galaxies. Galaxies with higher $M_{\star,100\text{kpc}}$ show more prominent stellar halos and have shallower outer μ_{\star} slopes. Assuming that stellar halos are dominated by accreted stars, this result is consistent with the two-phase formation picture of massive galaxies.

(iii) We show that, on average, massive galaxies have positive ellipticity gradients out to at least 60 kpc. The average ellipticity profile also depend on $M_{\star,100\text{kpc}}$: more massive galaxies tend to have steeper ellipticity gradients and become more elongated in stellar halos. On the other hand, the average $(g-r)$ and $(g-i)$ color gradients do not show clear dependence on $M_{\star,100\text{kpc}}$ within 10-60 kpc.

These results highlight the advantages of wide area, deep, and high-quality imaging for studying the evolution of massive galaxies. At present, the HSC survey has already doubled its sky coverage to ~ 200 deg², and provides a much larger sample of massive central galaxies. In the near future, we will extend this work to lower $M_{\star,100\text{kpc}}$ by using photometric redshifts, and we will also apply 2-D photometric methods (e.g. [Huang et al. 2013a](#)) to take advantage of the multi-wavelength nature of the HSC survey (e.g. [Huang et al. 2016b](#)). Our current work can also be combined with weak lensing measurements of the dark matter halos of massive galaxies and physical insights into the assembly histories of these galaxies can be gained by comparing with cosmological hydro-simulations such as Illustris ([Vogelsberger et al. 2014](#), [Genel et al. 2014](#)), EAGLE ([Schaye et al. 2015](#), [Crain et al. 2015](#)), or *Horizon-AGN* ([Dubois et al. 2014](#)).

ACKNOWLEDGEMENTS

The authors thank Rachel Mandelbaum and Frank van den Bosch for insightful discussions and comments; thank Shun Saito for helping us estimate the fraction of satellite galaxies in our sample; thank Feng-Shan Liu for sharing the μ_* profile of the $z \sim 1$ BCG from his work.

The Hyper Suprime-Cam (HSC) collaboration includes the astronomical communities of Japan and Taiwan, and Princeton University. The HSC instrumentation and software were developed by the National Astronomical Observatory of Japan (NAOJ), the Kavli Institute for the Physics and Mathematics of the Universe (Kavli IPMU), the University of Tokyo, the High Energy Accelerator Research Organization (KEK), the Academia Sinica Institute for Astronomy and Astrophysics in Taiwan (ASIAA), and Princeton University. Funding was contributed by the FIRST program from Japanese Cabinet Office, the Ministry of Education, Culture, Sports, Science and Technology (MEXT), the Japan Society for the Promotion of Science (JSPS), Japan Science and Technology Agency (JST), the Toray Science Foundation, NAOJ, Kavli IPMU, KEK, ASIAA, and Princeton University.

Funding for SDSS-III has been provided by the Alfred P. Sloan Foundation, the Participating Institutions, the National Science Foundation, and the U.S. Department of Energy. The SDSS-III web site is <http://www.sdss3.org>. SDSS-III is managed by the Astrophysical Research Consortium for the Participating Institutions of the SDSS-III Collaboration including the University of Arizona, the Brazilian Participation Group, Brookhaven National Laboratory, University of Cambridge, University of Florida, the French Participation Group, the German Participation Group, the Instituto de Astrofísica de Canarias, the Michigan State/Notre Dame/JINA Participation Group, Johns Hopkins University, Lawrence Berkeley National Laboratory, Max Planck Institute for Astrophysics, New Mexico State University, New York University, Ohio State University, Pennsylvania State University, University of Portsmouth, Princeton University, the Spanish Participation Group, University of Tokyo, University of Utah, Vanderbilt University, University of Virginia, University of Washington, and Yale University.

The Pan-STARRS1 Surveys (PS1) have been made possible through contributions of the Institute for Astronomy, the University of Hawaii, the Pan-STARRS Project Office, the Max-Planck Society and its participating institutes, the Max Planck Institute for Astronomy, Heidelberg and the Max Planck Institute for Extraterrestrial Physics, Garching, The Johns Hopkins University, Durham University, the University of Edinburgh, Queen's University Belfast, the Harvard-Smithsonian Center for Astrophysics, the Las Cumbres Observatory Global Telescope Network Incorporated, the National Central University of Taiwan, the Space Telescope Science Institute, the National Aeronautics and Space Administration under Grant No. NNX08AR22G issued through the Planetary Science Division of the NASA Science Mission Directorate, the National Science Foundation under Grant No. AST-1238877, the University of Maryland, and Eotvos Lorand University (ELTE).

This paper makes use of software developed for the Large Synoptic Survey Telescope. We thank the LSST

Project for making their code available as free software at <http://dm.lsstcorp.org>.

This research was supported in part by the National Science Foundation under Grant No. NSF PHY11-25915.

This research made use of: **STSCI_PYTHON**, a general astronomical data analysis infrastructure in Python. **STSCI_PYTHON** is a product of the Space Telescope Science Institute, which is operated by AURA for NASA; **SciPy**, an open source scientific tools for Python (Jones et al. 2001); **NumPy**, a fundamental package for scientific computing with Python (Walt et al. 2011); **Matplotlib**, a 2-D plotting library for Python (Hunter 2007); **Astropy**, a community-developed core Python package for Astronomy (Astropy Collaboration et al. 2013); **scikit-learn**, a machine-learning library in Python (Pedregosa et al. 2011); **astroML**, a machine learning library for astrophysics (Vanderplas et al. 2012); **IPython**, an interactive computing system for Python (Pérez & Granger 2007); **sep** Source Extraction and Photometry in Python (Barbary et al. 2015); **palettable**, color palettes for Python; **emcee**, Seriously Kick-Ass MCMC in Python; **Colossus**, COsmology, haLO and large-Scale StrUcture tools (Diemer 2015).

REFERENCES

- Abazajian K. N., et al., 2009, *ApJS*, **182**, 543
 Aihara H., et al., 2011, *ApJS*, **193**, 29
 Aihara H., et al., 2017a, preprint, ([arXiv:1702.08449](https://arxiv.org/abs/1702.08449))
 Aihara H., et al., 2017c, preprint, ([arXiv:1702.08449](https://arxiv.org/abs/1702.08449))
 Aihara H., et al., 2017b, preprint, ([arXiv:1704.05858](https://arxiv.org/abs/1704.05858))
 Alam S., et al., 2015a, *ApJS*, **219**, 12
 Alam S., et al., 2015b, *ApJS*, **219**, 12
 Annis J., et al., 2014, *ApJ*, **794**, 120
 Astropy Collaboration et al., 2013, *A&A*, **558**, A33
 Axelrod T., Kantor J., Lupton R. H., Pierfederici F., 2010, in *Software and Cyberinfrastructure for Astronomy*. p. 774015, [doi:10.1117/12.857297](https://doi.org/10.1117/12.857297)
 Barbary Boone Deil 2015, sep: v0.3.0, [doi:10.5281/zenodo.15669](https://doi.org/10.5281/zenodo.15669), <http://dx.doi.org/10.5281/zenodo.15669>
 Baugh C. M., Cole S., Frenk C. S., 1996, *MNRAS*, **283**, 1361
 Bédorf J., Portegies Zwart S., 2013, *MNRAS*, **431**, 767
 Belli S., Newman A. B., Ellis R. S., 2014, *ApJ*, **783**, 117
 Bender R., Kormendy J., Cornell M. E., Fisher D. B., 2015, *ApJ*, **807**, 56
 Bernardi M., Meert A., Sheth R. K., Vikram V., Huertas-Company M., Mei S., Shankar F., 2013, *MNRAS*, **436**, 697
 Bernardi M., Meert A., Sheth R. K., Fischer J.-L., Huertas-Company M., Maraston C., Shankar F., Vikram V., 2017, *MNRAS*, **467**, 2217
 Bezanson R., van Dokkum P. G., Tal T., Marchesini D., Kriek M., Franx M., Coppi P., 2009, *ApJ*, **697**, 1290
 Blanton M. R., Kazin E., Muna D., Weaver B. A., Price-Whelan A., 2011, *AJ*, **142**, 31
 Bosch J., et al., 2017, preprint, ([arXiv:1705.06766](https://arxiv.org/abs/1705.06766))
 Boylan-Kolchin M., Ma C.-P., Quataert E., 2008, *MNRAS*, **383**, 93
 Brainerd T. G., 2005, *ApJ*, **628**, L10
 Bundy K., et al., 2015, *ApJS*, **221**, 15
 Calzetti D., Armus L., Bohlin R. C., Kinney A. L., Koornneef J., Storchi-Bergmann T., 2000, *ApJ*, **533**, 682
 Capaccioli M., et al., 2015, *A&A*, **581**, A10
 Cappellari M., et al., 2012, *Nature*, **484**, 485
 Cappellari M., et al., 2013, *MNRAS*, **432**, 1862
 Carllberg R. G., Yee H. K. C., Ellingson E., 1997, *ApJ*, **478**, 462
 Carollo C. M., Danziger I. J., Buson L., 1993, *MNRAS*, **265**, 553

- Carter D., Bridges T. J., Hau G. K. T., 1999, *MNRAS*, **307**, 131
- Chabrier G., 2003, *PASP*, **115**, 763
- Chang Y.-Y., et al., 2013, *ApJ*, **773**, 149
- Cimatti A., et al., 2008, *A&A*, **482**, 21
- Clampitt J., Jain B., 2016, *MNRAS*, **457**, 4135
- Conroy C., Gunn J. E., 2010a, FSPS: Flexible Stellar Population Synthesis, Astrophysics Source Code Library (ascl:1010.043)
- Conroy C., Gunn J. E., 2010b, *ApJ*, **712**, 833
- Conroy C., van Dokkum P. G., 2012, *ApJ*, **760**, 71
- Cooper A. P., et al., 2010, *MNRAS*, **406**, 744
- Cooper A. P., D'Souza R., Kauffmann G., Wang J., Boylan-Kolchin M., Guo Q., Frenk C. S., White S. D. M., 2013, *MNRAS*, **434**, 3348
- Courteau S., Widrow L. M., McDonald M., Guhathakurta P., Gilbert K. M., Zhu Y., Beaton R. L., Majewski S. R., 2011, *ApJ*, **739**, 20
- Crain R. A., et al., 2015, *MNRAS*, **450**, 1937
- D'Souza R., Kauffman G., Wang J., Vegetti S., 2014, *MNRAS*, **443**, 1433
- D'Souza R., Vegetti S., Kauffmann G., 2015, *MNRAS*, **454**, 4027
- Davies R. L., Sadler E. M., Peletier R. F., 1993, *MNRAS*, **262**, 650
- De Lucia G., Springel V., White S. D. M., Croton D., Kauffmann G., 2006, *MNRAS*, **366**, 499
- Dekel A., Sari R., Ceverino D., 2009, *ApJ*, **703**, 785
- Diemer B., 2015, Colossus: COsmology, haLO, and large-Scale StrUcture toolS, Astrophysics Source Code Library (ascl:1501.016)
- Diemer B., Kravtsov A. V., 2015, *ApJ*, **799**, 108
- Dressler A., 1979, *ApJ*, **231**, 659
- Driver S. P., et al., 2011, *MNRAS*, **413**, 971
- Dubois Y., Gavazzi R., Peirani S., Silk J., 2013, *MNRAS*, **433**, 3297
- Dubois Y., et al., 2014, *MNRAS*, **444**, 1453
- Eisenstein D. J., et al., 2011, *AJ*, **142**, 72
- Fabian A. C., 2012, *ARA&A*, **50**, 455
- Falcón-Barroso J., Sánchez-Blázquez P., Vazdekis A., Ricciardelli E., Cardiel N., Cenarro A. J., Gorgas J., Peletier R. F., 2011, *A&A*, **532**, A95
- Farahi A., Evrard A. E., Rozo E., Rykoff E. S., Wechsler R. H., 2016, *MNRAS*, **460**, 3900
- Genel S., et al., 2014, *MNRAS*, **445**, 175
- Gonzalez A. H., Zabludoff A. I., Zaritsky D., 2005, *ApJ*, **618**, 195
- Graham A. W., 2013, Elliptical and Disk Galaxy Structure and Modern Scaling Laws. p. 91, doi:10.1007/978-94-007-5609-0_2
- Graham A. W., Guzmán R., 2003, *AJ*, **125**, 2936
- Harmsen B., Monachesi A., Bell E. F., de Jong R. S., Bailin J., Radburn-Smith D. J., Holwerda B. W., 2017, *MNRAS*, **466**, 1491
- Hilz M., Naab T., Ostriker J. P., Thomas J., Burkert A., Jesseit R., 2012, *MNRAS*, **425**, 3119
- Hilz M., Naab T., Ostriker J. P., 2013, *MNRAS*, **429**, 2924
- Hirata C. M., Mandelbaum R., Ishak M., Seljak U., Nichol R., Pimblet K. A., Ross N. P., Wake D., 2007, *MNRAS*, **381**, 1197
- Hirschmann M., Naab T., Ostriker J. P., Forbes D. A., Duc P.-A., Davé R., Oser L., Karabal E., 2015, *MNRAS*, **449**, 528
- Ho L. C., Li Z.-Y., Barth A. J., Seigar M. S., Peng C. Y., 2011, *ApJS*, **197**, 21
- Hopkins P. F., Hernquist L., Cox T. J., Dutta S. N., Rothberg B., 2008, *ApJ*, **679**, 156
- Hoshino H., et al., 2015, *MNRAS*, **452**, 998
- Huang S., Ho L. C., Peng C. Y., Li Z.-Y., Barth A. J., 2013a, *ApJ*, **766**, 47
- Huang S., Ho L. C., Peng C. Y., Li Z.-Y., Barth A. J., 2013b, *ApJ*, **768**, L28
- Huang H.-J., Mandelbaum R., Freeman P. E., Chen Y.-C., Rozo E., Rykoff E., Baxter E. J., 2016a, *MNRAS*, **463**, 222
- Huang S., Ho L. C., Peng C. Y., Li Z.-Y., Barth A. J., 2016b, *ApJ*, **821**, 114
- Huang S., et al., 2017, preprint, (arXiv:1705.01599)
- Hunter J. D., 2007, *Computing In Science & Engineering*, **9**, 90
- Iodice E., et al., 2016, *ApJ*, **820**, 42
- Iodice E., et al., 2017, *ApJ*, **839**, 21
- Jiang L., Cole S., Sawala T., Frenk C. S., 2015, *MNRAS*, **448**, 1674
- Jones E., Oliphant T., Peterson P., et al., 2001, SciPy: Open source scientific tools for Python, <http://www.scipy.org/>
- Jurić M., et al., 2015, preprint, (arXiv:1512.07914)
- Kauffmann G., et al., 2003, *MNRAS*, **341**, 54
- Kelson D. D., Zabludoff A. I., Williams K. A., Trager S. C., Mulchaey J. S., Bolte M., 2002, *ApJ*, **576**, 720
- Khandai N., Di Matteo T., Croft R., Wilkins S., Feng Y., Tucker E., DeGraf C., Liu M.-S., 2015, *MNRAS*, **450**, 1349
- Khochfar S., Silk J., 2006, *ApJ*, **648**, L21
- Kormendy J., Fisher D. B., Cornell M. E., Bender R., 2009, *ApJS*, **182**, 216
- Kriek M., et al., 2016, *Nature*, **540**, 248
- La Barbera F., De Carvalho R. R., De La Rosa I. G., Gal R. R., Swindle R., Lopes P. A. A., 2010, *AJ*, **140**, 1528
- La Barbera F., Ferreras I., de Carvalho R. R., Bruzual G., Charlot S., Pasquali A., Merlin E., 2012, *MNRAS*, **426**, 2300
- Lackner C. N., Cen R., Ostriker J. P., Joung M. R., 2012, *MNRAS*, **425**, 641
- Laporte C. F. P., White S. D. M., Naab T., Gao L., 2013, *MNRAS*, **435**, 901
- Lauer T. R., et al., 2007, *ApJ*, **664**, 226
- Lawrence A., et al., 2007, *MNRAS*, **379**, 1599
- Leauthaud A., et al., 2016, *MNRAS*, **457**, 4021
- Lee J., Yi S. K., 2013, *ApJ*, **766**, 38
- Lee J., Yi S. K., 2017, *ApJ*, **836**, 161
- Leja J., van Dokkum P., Franx M., 2013, *ApJ*, **766**, 33
- Li Z.-Y., Ho L. C., Barth A. J., Peng C. Y., 2011, *ApJS*, **197**, 22
- Lin Y.-T., Mohr J. J., 2004, *ApJ*, **617**, 879
- Liske J., et al., 2015, *MNRAS*, **452**, 2087
- Liu F. S., et al., 2013, *ApJ*, **769**, 147
- Longobardi A., Arnaboldi M., Gerhard O., Hanuschik R., 2015, *A&A*, **579**, A135
- Lupton R., Blanton M. R., Fekete G., Hogg D. W., O'Mullane W., Szalay A., Wherry N., 2004, *PASP*, **116**, 133
- Ma C.-P., Greene J. E., McConnell N., Janish R., Blakeslee J. P., Thomas J., Murphy J. D., 2014, *ApJ*, **795**, 158
- Magnier E. A., et al., 2013, *ApJS*, **205**, 20
- Meert A., Vikram V., Bernardi M., 2015, *MNRAS*, **446**, 3943
- Melchior P., et al., 2016, preprint, (arXiv:1610.06890)
- Mendel J. T., Simard L., Palmer M., Ellison S. L., Patton D. R., 2014, *ApJS*, **210**, 3
- Merritt A., van Dokkum P., Abraham R., Zhang J., 2016, *ApJ*, **830**, 62
- Mihos J. C., Harding P., Feldmeier J., Morrison H., 2005, *ApJ*, **631**, L41
- Mihos J. C., Harding P., Rudick C. S., Feldmeier J. J., 2013, *ApJ*, **764**, L20
- Mihos J. C., Harding P., Feldmeier J. J., Rudick C., Janowiecki S., Morrison H., Slater C., Watkins A., 2017, *ApJ*, **834**, 16
- Mitsuda K., Doi M., Morokuma T., Suzuki N., Yasuda N., Perlmutter S., Aldering G., Meyers J., 2017, *ApJ*, **834**, 109
- Miyazaki S., et al., 2012, in Ground-based and Airborne Instrumentation for Astronomy IV. p. 84460Z, doi:10.1117/12.926844
- Moustakas J., et al., 2013, *ApJ*, **767**, 50
- Murante G., Giovalli M., Gerhard O., Arnaboldi M., Borgani S., Dolag K., 2007, *MNRAS*, **377**, 2
- Naab T., Khochfar S., Burkert A., 2006, *ApJ*, **636**, L81
- Newman A. B., Ellis R. S., Bundy K., Treu T., 2012, *ApJ*, **746**, 162

Niederste-Ostholt M., Strauss M. A., Dong F., Koester B. P., McKay T. A., 2010, *MNRAS*, **405**, 2023
 Oh S., Greene J. E., Lackner C. N., 2017, *ApJ*, **836**, 115
 Oke J. B., Gunn J. E., 1983, *ApJ*, **266**, 713
 Oogi T., Habe A., 2013, *MNRAS*, **428**, 641
 Oser L., Ostriker J. P., Naab T., Johansson P. H., Burkert A., 2010, *ApJ*, **725**, 2312
 Oser L., Naab T., Ostriker J. P., Johansson P. H., 2012, *ApJ*, **744**, 63
 Patel S. G., et al., 2013, *ApJ*, **766**, 15
 Pedregosa F., et al., 2011, *Journal of Machine Learning Research*, **12**, 2825
 Pérez F., Granger B. E., 2007, *Computing in Science and Engineering*, **9**, 21
 Porter A. C., Schneider D. P., Hoessel J. G., 1991, *AJ*, **101**, 1561
 Qu Y., et al., 2017, *MNRAS*, **464**, 1659
 Reid B. A., Seo H.-J., Leauthaud A., Tinker J. L., White M., 2014, *MNRAS*, **444**, 476
 Ricciardelli E., Vazdekis A., Cenarro A. J., Falcón-Barroso J., 2012, *MNRAS*, **424**, 172
 Rodríguez S., Padilla N. D., 2013, *MNRAS*, **434**, 2153
 Rodriguez-Gomez V., et al., 2016, *MNRAS*, **458**, 2371
 Rozo E., Rykoff E. S., 2014, *ApJ*, **783**, 80
 Rozo E., Rykoff E. S., Bartlett J. G., Melin J.-B., 2015a, *MNRAS*, **450**, 592
 Rozo E., Rykoff E. S., Becker M., Reddick R. M., Wechsler R. H., 2015b, *MNRAS*, **453**, 38
 Rykoff E. S., et al., 2014, *ApJ*, **785**, 104
 Saito S., et al., 2016, *MNRAS*, **460**, 1457
 Salpeter E. E., 1955, *ApJ*, **121**, 161
 Sánchez-Blázquez P., et al., 2006, *MNRAS*, **371**, 703
 Saro A., et al., 2015, *MNRAS*, **454**, 2305
 Schaye J., et al., 2015, *MNRAS*, **446**, 521
 Schlafly E. F., Finkbeiner D. P., 2011, *ApJ*, **737**, 103
 Schlafly E. F., et al., 2012, *ApJ*, **756**, 158
 Schombert J. M., 2015, *AJ*, **150**, 162
 Shin T.-h., Clampitt J., Jain B., Bernstein G., Neil A., Rozo E., Rykoff E., 2017, preprint, ([arXiv:1705.11167](https://arxiv.org/abs/1705.11167))
 Sijacki D., Springel V., Di Matteo T., Hernquist L., 2007, *MNRAS*, **380**, 877
 Simet M., McClintock T., Mandelbaum R., Rozo E., Rykoff E., Sheldon E., Wechsler R. H., 2016, preprint, ([arXiv:1603.06953](https://arxiv.org/abs/1603.06953))
 Spavone M., et al., 2017, preprint, ([arXiv:1703.10835](https://arxiv.org/abs/1703.10835))
 Szomoru D., Franx M., van Dokkum P. G., 2012, *ApJ*, **749**, 121
 Tal T., van Dokkum P. G., 2011, *ApJ*, **731**, 89
 Taylor E. N., et al., 2011, *MNRAS*, **418**, 1587
 Tonry J. L., et al., 2012, *ApJ*, **750**, 99
 Tremblay B., Merritt D., 1995, *AJ*, **110**, 1039
 Tremblay B., Merritt D., 1996, *AJ*, **111**, 2243
 Trujillo I., et al., 2006, *MNRAS*, **373**, L36
 Vanderplas J., Connolly A., Ivezić Ž., Gray A., 2012, in *Conference on Intelligent Data Understanding (CIDU)*. pp 47–54, [doi:10.1109/CIDU.2012.6382200](https://doi.org/10.1109/CIDU.2012.6382200)
 Vogelsberger M., et al., 2014, *MNRAS*, **444**, 1518
 Walcher J., Groves B., Budavári T., Dale D., 2011, *Ap&SS*, **331**, 1
 Walt S. v. d., Colbert S. C., Varoquaux G., 2011, *Computing in Science and Engg.*, **13**, 22
 Weijmans A.-M., et al., 2014, *MNRAS*, **444**, 3340
 Wetzell A. R., 2011, *MNRAS*, **412**, 49
 Wu H., Shao Z., Mo H. J., Xia X., Deng Z., 2005, *ApJ*, **622**, 244
 Wu X., Gerhard O., Naab T., Oser L., Martinez-Valpuesta I., Hilz M., Churazov E., Lyskova N., 2014, *MNRAS*, **438**, 2701
 Yang X., van den Bosch F. C., Mo H. J., Mao S., Kang X., Weinmann S. M., Guo Y., Jing Y. P., 2006, *MNRAS*, **369**, 1293
 Yang X., Mo H. J., van den Bosch F. C., Pasquali A., Li C., Barden M., 2007, *ApJ*, **671**, 153

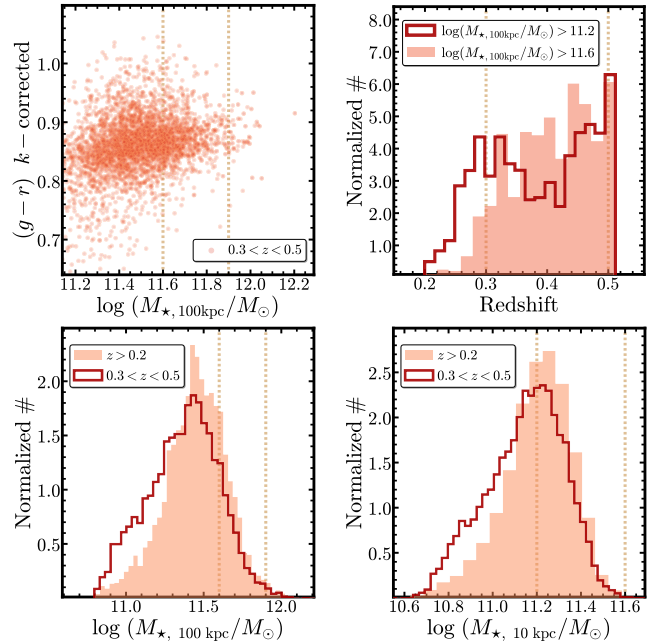


Figure 1. **Top-left:** The $\log(M_{\star,100\text{kpc}}/M_{\odot})$ - $(g-r)$ rest-frame color relation for the HSC massive galaxies. We k -correct the color using the *i*SEDFit fitting results. Massive galaxies form a “red-sequence” on this figure, and there is little contamination from blue object at high-mass end. **Top-right:** the redshift distribution of the massive galaxies. The filled and empty histograms are for the $\log(M_{\star,100\text{kpc}}/M_{\odot}) > 11.2$ and $\log(M_{\star,100\text{kpc}}/M_{\odot}) > 11.6$ galaxies. The vertical lines highlights the $0.3 \leq z \leq 0.5$ redshift range. **Bottom-left:** the distributions of $M_{\star,100\text{kpc}}$ of massive galaxies in this sample. Filled histogram shows the distribution for $0.3 < z < 0.5$ galaxies used in this work. And the empty histogram shows the distribution for the whole $z > 0.2$ sample as comparison. **Bottom-right:** the distributions of $M_{\star,10\text{kpc}}$ in similar format.

Zibetti S., White S. D. M., Schneider D. P., Brinkmann J., 2005, *MNRAS*, **358**, 949
 van Dokkum P. G., et al., 2008, *ApJ*, **677**, L5
 van Dokkum P. G., et al., 2010, *ApJ*, **709**, 1018
 van Uitert E., et al., 2016, *MNRAS*, **459**, 3251
 van de Sande J., et al., 2011, *ApJ*, **736**, L9
 van der Wel A., et al., 2011, *ApJ*, **730**, 38
 van der Wel A., et al., 2014, *ApJ*, **788**, 28

APPENDIX A: A. BASIC STATISTICAL PROPERTIES OF THE SAMPLE

Here we show the basic statistics of the massive galaxies used in this work. On the top-left panel of Fig 1, we show the $M_{\star,100\text{kpc}}$ -color relation using the k -corrected rest-frame $(g-r)$ color. These massive galaxies form a clear “red-sequence” with little contamination from the “blue cloud” at the very high-mass end.

In the rest of Fig 1, we also show the distributions of redshift, $M_{\star,100\text{kpc}}$, and $M_{\star,10\text{kpc}}$. In this work, we focus on the massive galaxies with $\log(M_{\star,100\text{kpc}}/M_{\odot}) > 11.6$ at $0.3 < z < 0.5$ where the sample is fairly complete in $M_{\star,100\text{kpc}}$.

APPENDIX B: B. EXTRACTION OF 1-D SURFACE BRIGHTNESS PROFILE

Here we briefly discuss a few technical issues related to the measurements of the 1-D surface brightness profiles around massive galaxies.

To derive reliable 1-D profile, it is important to mask out all the irrelevant objects around the target. At the depth of the HSC images, this becomes a challenging task, especially for massive galaxies with extended outer profiles and many satellites. At this point, the `hscPipe` tends to over-subtract the background around bright objects. The performance of its deblending process is also not optimized for extended objects. For these reasons, we perform `SExtractor`-like background subtraction and object detection using the `SEP` Python library to generate the necessary masks. Combining two different local background models and S/N thresholds, we obtain the centroid, shape, and radius that enclose 90% of flux for each object, including the one that is very close to the center of bright galaxy (left panel of Fig B1). Based on these information, we then create the mask that covers all contaminating objects around the target after adaptively increasing the sizes of their masks according to their brightness and distance to the central target. Generally speaking, we mask out bright objects or objects in the outskirts of the image more aggressively to reduce their impact on the surface brightness profiles in the outskirts. We also create masks that are less and more aggressive than the default one to test their impacts on the surface brightness profiles.

Next, we aggressively mask out all objects on the cut-out image. We then evaluate the background level using the unmasked pixels after median smoothing the masked image using box of 6x6 pixels. This provides estimate of global background level along with its uncertainty. Given the typical background uncertainty, the HSC WIDE image should be able to reach down to > 29 mag arcsec⁻² surface brightness level in the i -band. However, as mentioned, we often find evidence of slightly over-subtracted background for massive galaxies in our sample. In the current `hscPipe`, the background on each CCD is modeled with a Chebyshev-polynomial that is fit to the smoothed image after excluding pixels with $S/N > 5$. This algorithm performs much better than the SDSS version (e.g. see Blanton et al. 2011), yet still over-subtracts background around bright objects and results in unphysical truncation in their surface brightness profiles. We empirically correct this issue using the background model generated by the `SExtractor` algorithm on the masked image (200x200 pixels background box size, and 6 pixels median filtering size of sky boxes). This model can account for the slightly over-subtracted background at large scale, and reduce the impact from the low surface brightness “wings” of bright neighbors. We clearly see improvement in both the distributions of background pixels (more symmetric distribution; median value is closer to 0) and the surface brightness profile (middle panel of Fig B; the negative intensity and the turn-over of the curve-of-growth in the outskirts of the “Original” profile are successfully corrected) after this correction. Also, it is worth mentioning that such correction does not often affect the surface brightness profile within 100 kpc.

The procedure used to derive 1-D surface bright-

ness profile from the background-corrected, contamination-masked images is already described in § 3 briefly. In practice, the profile at very low surface brightness level is sensitive to several `Ellipse` configurations. After some tests, we choose to use 0.1 dex in logarithm as the step in semi-major axis length between successive ellipses, and we use the median pixel value over the elliptical annulus after rejecting outlying pixels via 3σ -clipping three times. We make the above choices to make the final profile less affected by any nearby object, and also test the differences between the profiles derived using larger step, or mean value on the annulus, or fewer times of σ -clipping. Generally speaking, the surface brightness profile is very robust against these changes, especially within 100 kpc. On the right panel of Fig B1, we compare the surface brightness profiles for an example massive galaxy using different masks and `Ellipse` parameters. The profile within 100 kpc is very stable, and the only noticeable difference is caused by the less aggressive object-mask in the very outskirts.

We should also mention that we run `Ellipse` allowing for more sophisticated shapes than simple ellipse (4th Fourier modes that can make isophote more “disky” or “boxy”, e.g. Kormendy et al. 2009) to fit the isophote better. We also apply the isophotes from i -band images to other bands in “force-photometry” mode `Ellipse` run to get initial estimates of color profiles.

APPENDIX C: C. ESTIMATE AVERAGE M_\star/L_\star USING ISEDFIT

In § 4.1, we briefly explain the SED fitting procedure and the priors used. In Fig ??, we show an example of the `iSEDFit` output by visualizing the 5-band HSC SED on top of the best-fit model along with the PDF of the key parameters.

Although we only use the best-fit M_\star/L_\star in this work, it is necessary to make sure the model is reasonable. We show the relations between M_\star and a few key stellar population parameters derived by `iSEDFit` in Fig C2. Degeneracies among these parameters are inevitable based on only five broad-band photometry, but as expected, most massive galaxies show old stellar age, high stellar metallicity ($1.5 \times Z_\odot$ is the highest metallicity allowed by the adopted `FSPS` SSP models), and low dust extinction.

Meanwhile, M_\star measurement based on SED fitting heavily depends on the adopted SSP model, the form of IMF, dust extinction law, and details in the assumption of SFH (e.g. Bernardi et al. 2017). For massive galaxies in this sample, the form of the SFH²⁰, the contribution from random star burst²¹ rarely affect the M_\star . But the choices of SSP model, IMF, and dust extinction do systematically impact

²⁰ We choose to use the delayed- τ model for SFH; we adopt flat distribution between 0.5 to 14.0 Gyrs as the prior for the look-back time when the star formation turned on. The exponential delayed time-scale (τ) is allowed to change between 0.1 to 3.0 with equal probability

²¹ The chance of random star burst is set at 0.2 for every 2 Gyrs. The duration of the star burst is draw from a logarithmic distribution between 0.03 to 0.3 Gyr; and the mass fraction formed in the burst is from a logarithmic distribution between 0.01 and 1.0.

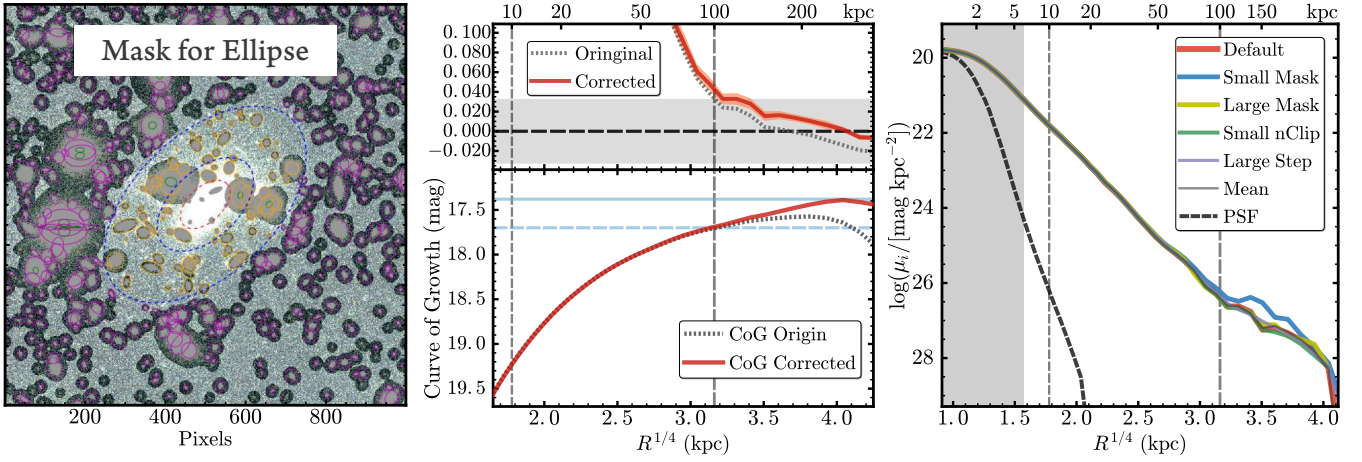


Figure B1. **Left:** Example of the object-mask built for the *Ellipse* run for a typical massive galaxy in the sample. All the shaded regions are masked out. The three dash lines (red, inner one and two blue ones) around the target at the center outlines the three radius we defined using the flux radius of the target. We increase the mask size for objects detected in different regions separated by these apertures (which are outlined by solid, elliptical apertures with different colors) using slightly different criteria. **Middle:** The zoom-in intensity profile around very low intensity value (top panel), and the curve-of-growth of the enclosed magnitude (bottom panel) of the example galaxy. To highlight the importance of background correction, we show the profiles using both images with (red, solid line) and without (black, dotted line) background correction. On the top panel, besides the horizontal line that highlights the zero flux level, we also show the uncertainty of the sky background estimate using the grey-shaded region. On the bottom panel, two horizontal lines indicate the magnitudes corresponding to total flux (solid) and flux within 100 kpc (dash). **Right:** compares the 1-D surface brightness profiles for the same example galaxy using different masks (smaller masking region: red, dash line; larger masks: blue, dash line), or different *Ellipse* configurations (more aggressive pixel-clipping: cyan, dash line; larger step in radius: green, dash line; using mean flux along the isophote instead of median: purple, dash line) with the default one (black, solid line).

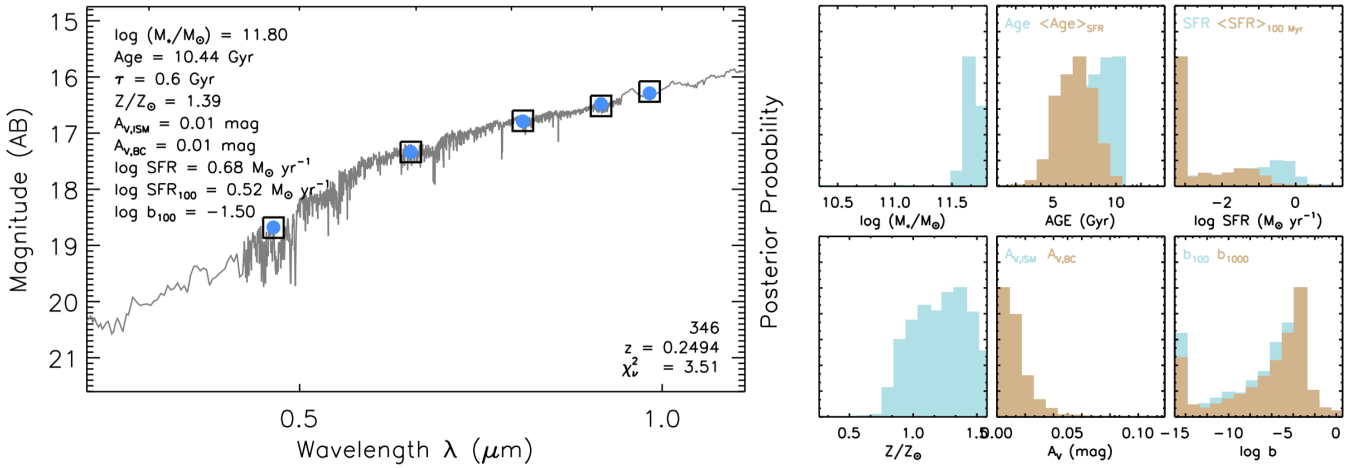


Figure C1. **Left:** Example of output figure from *iSEDfit* that shows the SED fitting results. The open-boxes show the observed fluxes in 5-band, and the solid, blue-dots show the best-fitted results, along with the high-resolution spectrum for this model reconstructed using the synthetic spectra from *FSPS*. Top-left corner shows the best-fit stellar population parameters, and bottom-right corner shows the ID, redshift of this object, and reduced χ^2 of the best-fit model. **Right:** the Posterior distributions of a few key parameters. From top-left to bottom right are: 1) stellar mass ($\log(M_\star/M_\odot)$); 2) age of the population (mass and star-formation rate weighted) in Gyr; 3) star formation rate ($\log \text{SFR} (M_\odot/\text{yr})$); instant one and the one averaged over the previous 100 Myr; 4) stellar metallicity (Z/Z_\odot); 5) dust extinction (A_V in mag); 6) birthrate parameter ($\log b$; averaged over previous 100 and 1000 Myr).

the estimates of M_\star , and therefore we look into this with a few additional tests (see Fig C3):

(i) Choosing the [Salpeter \(1955\)](#) IMF results in systematically higher M_\star (on average +0.25 dex of $\log(M_\star/M_\odot)$) for these massive galaxies (top panel). Although there are

multiple lines of evidence that favor Salpeter or even more “bottom-heavy” IMF in massive galaxies (e.g. [Conroy & van Dokkum 2012](#); [Cappellari et al. 2012](#)), we still present the main results using Chabrier IMF to accommodate galaxies with lower M_\star in the sample, and to be as consistent as

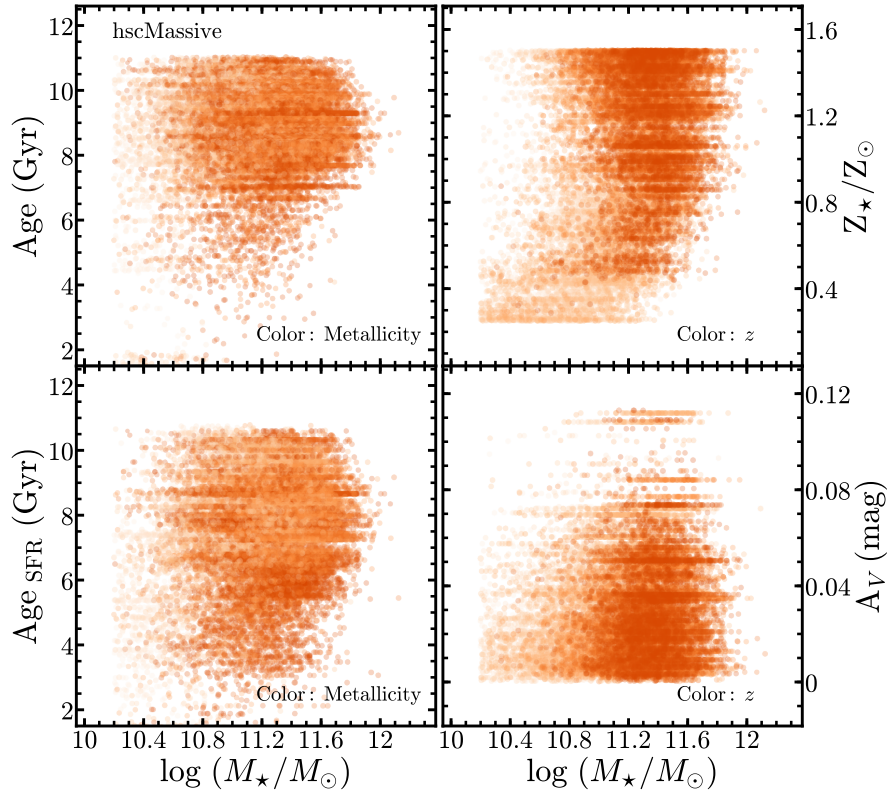


Figure C2. Relationships between M_\star and key stellar population parameters from `iSEDfit`. The four stellar population properties are: 1) **Top-left:** M_\star -weighted stellar population age in Gyr; 2) **Bottom-left:** SFR-weighted age in Gyr; 3) **Top-right:** M_\star -weighted stellar metallicity in unit of Solar value; 4) **bottom-right:** dust extinction value in V-band. As expected, most of the HSC massive galaxies are old, metal-rich, and dust-free.

possible with previous works. This choice of IMF does not change the main results qualitatively.

(ii) M_\star based on the BC03 models are systematically lower than the ones based on FSPS+MILES models (middle panel). The difference shows a large scatter, and can be as large as 0.4 dex, although it is not M_\star -dependent. The BC03 results show better average χ^2 than the FSPS ones. This relates to the higher upper-limit of stellar metallicity ($2 \times Z_\odot$) allowed by the BC03 model, which help fits the shape of the SED in the red-end slightly better. However, the BC03 results also show puzzlingly low stellar ages ($< 3-4$ Gyrs) for these massive, red galaxies. This could also lead to underestimated M_\star/L_\star values. It is worth noting that, both FSPS and BC03 models still have difficulties recovering SED at the very red-end (between z and y -band), and reproducing the optical color-color relations for red-sequence galaxies (e.g. [Ricciardelli et al. 2012](#)). In this work, we decide to keep using the FSPS+MILES model as the fiducial one. Using results based on BC03 model will not change any of our conclusions here.

(iii) On the bottom panel of Fig C3, we compare with the SED fitting results without considering the dust extinction. This choice leads to slightly smaller M_\star values as expected. Its impact becomes slightly larger at lower M_\star end. It will not change any of our conclusions here.

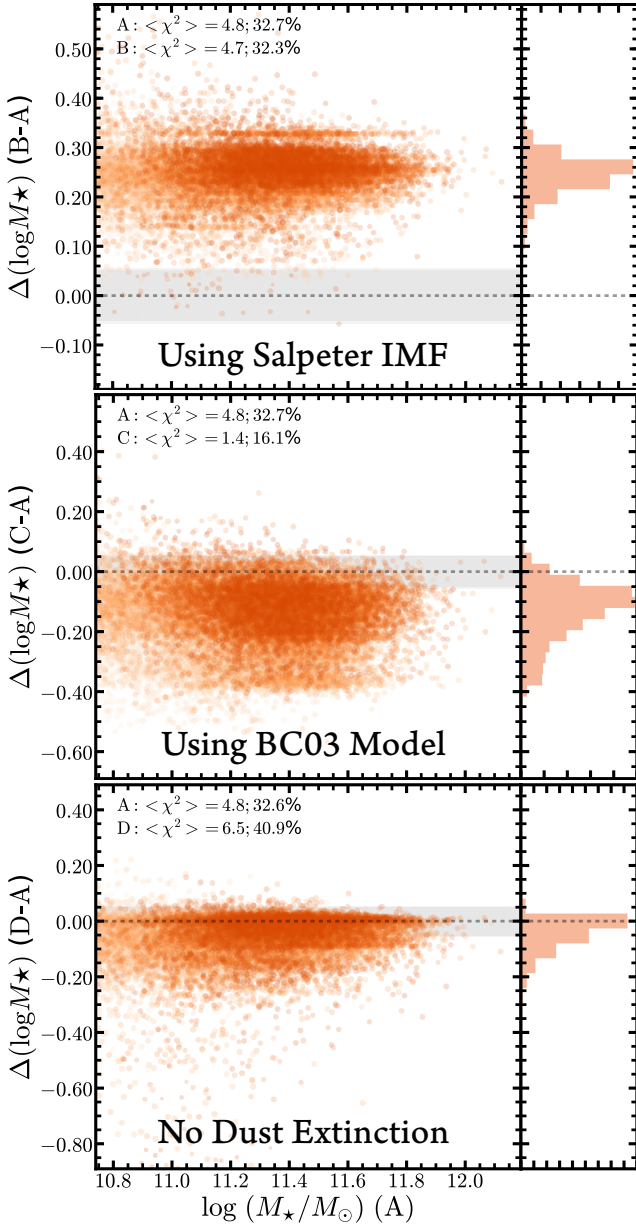


Figure C3. Comparisons of M_\star estimated by *iSEDFit* using different model assumptions. In each figure, we plot the M_\star from the default model against the differences with other models. The four models involved are labeled as: (A): Default model; (B): Using the Salpeter IMF instead of the Chabrier one (**Top panel**); (C): Using the BC03 synthetic population model instead of the FSPS one (**Middle panel**); (D): No dust extinction (**Bottom panel**). On each panel, the grey shaded region highlights the typical uncertainty of the $\log(\log(M_\star/M_\odot))$. For each pair of models, we highlight their median χ^2 values and the fraction of galaxies with $\chi^2 > 10.0$ at the top. On each panel, we also show the histograms of the M_\star -differences on the right side.

Table 1. Average μ_\star Profiles of Massive Galaxies in Different Stellar Mass Bins

Radius kpc	$[\mu_\star]$; Combined samples			$[\mu_\star]$; $M_{\star,100}$ kpc-matched		$[\mu_\star]$; $M_{\star,10}$ kpc-matched	
	$\log(M_\odot/\text{kpc}^2)$			$\log(M_\odot/\text{kpc}^2)$		$\log(M_\odot/\text{kpc}^2)$	
	$\log \frac{M_{\star,100\text{kpc}}}{M_\odot} \in [11.4, 11.6]$	[11.6, 11.8]	[11.8, 12.0]	cenHighMh	cenLowMh	cenHighMh	cenLowMh
(1)	(2)	(3)	(4)	(5)	(6)	(7)	(8)
0.0	9.23 ^{+0.00} _{-0.00}	9.31 ^{+0.00} _{-0.00}	9.32 ^{+0.01} _{-0.01}	9.31 ^{+0.02} _{-0.02}	9.34 ^{+0.01} _{-0.01}	9.31 ^{+0.02} _{-0.02}	9.34 ^{+0.02} _{-0.02}
0.6	9.20 ^{+0.00} _{-0.00}	9.28 ^{+0.00} _{-0.00}	9.29 ^{+0.01} _{-0.01}	9.27 ^{+0.02} _{-0.02}	9.31 ^{+0.01} _{-0.01}	9.28 ^{+0.02} _{-0.02}	9.31 ^{+0.02} _{-0.02}
1.0	9.16 ^{+0.00} _{-0.00}	9.24 ^{+0.00} _{-0.00}	9.26 ^{+0.01} _{-0.01}	9.24 ^{+0.02} _{-0.02}	9.27 ^{+0.01} _{-0.01}	9.25 ^{+0.02} _{-0.02}	9.27 ^{+0.02} _{-0.02}
1.4	9.12 ^{+0.00} _{-0.00}	9.20 ^{+0.00} _{-0.00}	9.23 ^{+0.01} _{-0.01}	9.20 ^{+0.02} _{-0.02}	9.23 ^{+0.01} _{-0.01}	9.21 ^{+0.02} _{-0.02}	9.23 ^{+0.02} _{-0.02}
1.7	9.06 ^{+0.00} _{-0.00}	9.15 ^{+0.00} _{-0.00}	9.19 ^{+0.01} _{-0.01}	9.15 ^{+0.02} _{-0.02}	9.19 ^{+0.01} _{-0.01}	9.16 ^{+0.01} _{-0.01}	9.18 ^{+0.01} _{-0.01}
2.0	9.00 ^{+0.00} _{-0.00}	9.10 ^{+0.00} _{-0.00}	9.15 ^{+0.01} _{-0.01}	9.09 ^{+0.02} _{-0.02}	9.13 ^{+0.01} _{-0.01}	9.11 ^{+0.01} _{-0.01}	9.12 ^{+0.01} _{-0.01}
2.4	8.93 ^{+0.00} _{-0.00}	9.03 ^{+0.00} _{-0.00}	9.09 ^{+0.01} _{-0.01}	9.03 ^{+0.02} _{-0.02}	9.07 ^{+0.01} _{-0.01}	9.05 ^{+0.01} _{-0.01}	9.05 ^{+0.01} _{-0.01}
2.7	8.87 ^{+0.00} _{-0.00}	8.97 ^{+0.00} _{-0.00}	9.04 ^{+0.01} _{-0.01}	8.97 ^{+0.01} _{-0.01}	9.01 ^{+0.01} _{-0.01}	9.00 ^{+0.01} _{-0.01}	8.99 ^{+0.01} _{-0.01}
3.0	8.80 ^{+0.00} _{-0.00}	8.90 ^{+0.00} _{-0.00}	8.98 ^{+0.01} _{-0.01}	8.90 ^{+0.01} _{-0.01}	8.95 ^{+0.01} _{-0.01}	8.93 ^{+0.01} _{-0.01}	8.92 ^{+0.01} _{-0.01}
3.4	8.72 ^{+0.00} _{-0.00}	8.83 ^{+0.00} _{-0.00}	8.92 ^{+0.01} _{-0.01}	8.83 ^{+0.01} _{-0.01}	8.88 ^{+0.01} _{-0.01}	8.86 ^{+0.01} _{-0.01}	8.85 ^{+0.01} _{-0.01}
3.7	8.66 ^{+0.00} _{-0.00}	8.78 ^{+0.00} _{-0.00}	8.87 ^{+0.01} _{-0.01}	8.78 ^{+0.01} _{-0.01}	8.83 ^{+0.01} _{-0.01}	8.81 ^{+0.01} _{-0.01}	8.79 ^{+0.01} _{-0.01}
4.1	8.60 ^{+0.00} _{-0.00}	8.72 ^{+0.00} _{-0.00}	8.82 ^{+0.01} _{-0.01}	8.72 ^{+0.01} _{-0.01}	8.77 ^{+0.01} _{-0.01}	8.76 ^{+0.01} _{-0.01}	8.73 ^{+0.01} _{-0.01}
4.4	8.54 ^{+0.00} _{-0.00}	8.66 ^{+0.00} _{-0.00}	8.77 ^{+0.01} _{-0.01}	8.66 ^{+0.01} _{-0.01}	8.72 ^{+0.01} _{-0.01}	8.70 ^{+0.01} _{-0.01}	8.67 ^{+0.01} _{-0.01}
4.8	8.48 ^{+0.00} _{-0.00}	8.60 ^{+0.00} _{-0.00}	8.71 ^{+0.01} _{-0.01}	8.60 ^{+0.01} _{-0.01}	8.66 ^{+0.01} _{-0.01}	8.65 ^{+0.01} _{-0.01}	8.61 ^{+0.01} _{-0.01}
6.2	8.26 ^{+0.00} _{-0.00}	8.40 ^{+0.00} _{-0.00}	8.53 ^{+0.01} _{-0.01}	8.41 ^{+0.01} _{-0.01}	8.46 ^{+0.01} _{-0.01}	8.46 ^{+0.02} _{-0.02}	8.40 ^{+0.02} _{-0.02}
7.6	8.09 ^{+0.00} _{-0.00}	8.24 ^{+0.00} _{-0.00}	8.39 ^{+0.01} _{-0.01}	8.27 ^{+0.01} _{-0.01}	8.31 ^{+0.01} _{-0.01}	8.31 ^{+0.02} _{-0.02}	8.23 ^{+0.02} _{-0.02}
9.0	7.95 ^{+0.00} _{-0.00}	8.10 ^{+0.00} _{-0.00}	8.27 ^{+0.01} _{-0.01}	8.14 ^{+0.02} _{-0.02}	8.18 ^{+0.01} _{-0.01}	8.19 ^{+0.02} _{-0.02}	8.09 ^{+0.02} _{-0.02}
10.3	7.82 ^{+0.00} _{-0.00}	7.99 ^{+0.00} _{-0.00}	8.16 ^{+0.01} _{-0.01}	8.03 ^{+0.02} _{-0.02}	8.06 ^{+0.01} _{-0.01}	8.09 ^{+0.02} _{-0.02}	7.97 ^{+0.02} _{-0.02}
11.7	7.70 ^{+0.00} _{-0.00}	7.88 ^{+0.00} _{-0.00}	8.06 ^{+0.01} _{-0.01}	7.93 ^{+0.02} _{-0.02}	7.96 ^{+0.01} _{-0.01}	7.99 ^{+0.02} _{-0.02}	7.85 ^{+0.02} _{-0.02}
13.0	7.60 ^{+0.00} _{-0.00}	7.78 ^{+0.00} _{-0.00}	7.98 ^{+0.01} _{-0.01}	7.85 ^{+0.02} _{-0.02}	7.87 ^{+0.01} _{-0.01}	7.90 ^{+0.02} _{-0.02}	7.75 ^{+0.02} _{-0.02}
14.5	7.50 ^{+0.00} _{-0.00}	7.69 ^{+0.00} _{-0.00}	7.90 ^{+0.01} _{-0.01}	7.76 ^{+0.02} _{-0.02}	7.78 ^{+0.01} _{-0.01}	7.82 ^{+0.02} _{-0.02}	7.65 ^{+0.02} _{-0.02}
16.0	7.39 ^{+0.00} _{-0.00}	7.60 ^{+0.00} _{-0.00}	7.82 ^{+0.01} _{-0.01}	7.68 ^{+0.02} _{-0.02}	7.69 ^{+0.01} _{-0.01}	7.74 ^{+0.02} _{-0.02}	7.56 ^{+0.02} _{-0.02}
17.3	7.31 ^{+0.00} _{-0.00}	7.52 ^{+0.00} _{-0.00}	7.76 ^{+0.01} _{-0.01}	7.61 ^{+0.02} _{-0.02}	7.62 ^{+0.01} _{-0.01}	7.67 ^{+0.03} _{-0.03}	7.48 ^{+0.03} _{-0.03}
18.7	7.23 ^{+0.00} _{-0.00}	7.45 ^{+0.00} _{-0.00}	7.69 ^{+0.01} _{-0.01}	7.55 ^{+0.02} _{-0.02}	7.55 ^{+0.01} _{-0.01}	7.61 ^{+0.03} _{-0.03}	7.40 ^{+0.03} _{-0.03}
22.6	7.02 ^{+0.00} _{-0.00}	7.27 ^{+0.00} _{-0.00}	7.54 ^{+0.01} _{-0.01}	7.38 ^{+0.02} _{-0.02}	7.37 ^{+0.01} _{-0.01}	7.45 ^{+0.03} _{-0.03}	7.21 ^{+0.03} _{-0.03}
26.1	6.86 ^{+0.00} _{-0.00}	7.12 ^{+0.00} _{-0.00}	7.41 ^{+0.01} _{-0.01}	7.25 ^{+0.02} _{-0.02}	7.24 ^{+0.01} _{-0.01}	7.32 ^{+0.03} _{-0.03}	7.05 ^{+0.03} _{-0.03}
30.0	6.70 ^{+0.00} _{-0.00}	6.98 ^{+0.00} _{-0.00}	7.29 ^{+0.01} _{-0.01}	7.13 ^{+0.03} _{-0.03}	7.10 ^{+0.01} _{-0.01}	7.20 ^{+0.03} _{-0.03}	6.90 ^{+0.03} _{-0.03}
33.7	6.55 ^{+0.00} _{-0.00}	6.85 ^{+0.00} _{-0.00}	7.18 ^{+0.01} _{-0.01}	7.01 ^{+0.02} _{-0.02}	6.98 ^{+0.01} _{-0.01}	7.09 ^{+0.04} _{-0.04}	6.76 ^{+0.04} _{-0.04}
37.8	6.41 ^{+0.00} _{-0.00}	6.72 ^{+0.00} _{-0.00}	7.07 ^{+0.01} _{-0.01}	6.90 ^{+0.03} _{-0.03}	6.85 ^{+0.01} _{-0.01}	6.98 ^{+0.04} _{-0.04}	6.63 ^{+0.04} _{-0.04}
41.6	6.29 ^{+0.01} _{-0.01}	6.61 ^{+0.01} _{-0.01}	6.98 ^{+0.01} _{-0.01}	6.81 ^{+0.03} _{-0.03}	6.75 ^{+0.01} _{-0.01}	6.89 ^{+0.04} _{-0.04}	6.51 ^{+0.04} _{-0.04}
45.7	6.17 ^{+0.01} _{-0.01}	6.50 ^{+0.01} _{-0.01}	6.88 ^{+0.01} _{-0.01}	6.71 ^{+0.03} _{-0.03}	6.64 ^{+0.01} _{-0.01}	6.79 ^{+0.04} _{-0.04}	6.39 ^{+0.04} _{-0.04}
49.3	6.07 ^{+0.01} _{-0.01}	6.41 ^{+0.01} _{-0.01}	6.80 ^{+0.01} _{-0.01}	6.62 ^{+0.03} _{-0.03}	6.56 ^{+0.01} _{-0.01}	6.70 ^{+0.04} _{-0.04}	6.30 ^{+0.04} _{-0.04}
53.1	5.98 ^{+0.01} _{-0.01}	6.33 ^{+0.01} _{-0.01}	6.71 ^{+0.01} _{-0.01}	6.55 ^{+0.03} _{-0.03}	6.46 ^{+0.01} _{-0.01}	6.64 ^{+0.04} _{-0.04}	6.21 ^{+0.04} _{-0.04}
57.2	5.88 ^{+0.01} _{-0.01}	6.24 ^{+0.01} _{-0.01}	6.63 ^{+0.02} _{-0.02}	6.47 ^{+0.04} _{-0.04}	6.37 ^{+0.01} _{-0.01}	6.56 ^{+0.04} _{-0.04}	6.11 ^{+0.04} _{-0.04}
61.5	5.79 ^{+0.01} _{-0.01}	6.15 ^{+0.01} _{-0.01}	6.55 ^{+0.02} _{-0.02}	6.39 ^{+0.04} _{-0.04}	6.29 ^{+0.01} _{-0.01}	6.49 ^{+0.04} _{-0.04}	6.03 ^{+0.04} _{-0.04}
66.0	5.70 ^{+0.01} _{-0.01}	6.05 ^{+0.01} _{-0.01}	6.47 ^{+0.02} _{-0.02}	6.32 ^{+0.04} _{-0.04}	6.20 ^{+0.01} _{-0.01}	6.37 ^{+0.05} _{-0.05}	5.94 ^{+0.05} _{-0.05}
69.8	5.64 ^{+0.01} _{-0.01}	5.98 ^{+0.01} _{-0.01}	6.40 ^{+0.02} _{-0.02}	6.25 ^{+0.04} _{-0.04}	6.12 ^{+0.02} _{-0.02}	6.35 ^{+0.04} _{-0.04}	5.87 ^{+0.04} _{-0.04}
74.7	5.56 ^{+0.01} _{-0.01}	5.89 ^{+0.01} _{-0.01}	6.32 ^{+0.02} _{-0.02}	6.18 ^{+0.04} _{-0.04}	6.04 ^{+0.02} _{-0.02}	6.28 ^{+0.05} _{-0.05}	5.79 ^{+0.05} _{-0.05}
79.9	5.49 ^{+0.01} _{-0.01}	5.81 ^{+0.01} _{-0.01}	6.24 ^{+0.02} _{-0.02}	6.12 ^{+0.04} _{-0.04}	5.96 ^{+0.02} _{-0.02}	6.20 ^{+0.05} _{-0.05}	5.72 ^{+0.05} _{-0.05}
84.3	5.43 ^{+0.01} _{-0.01}	5.74 ^{+0.01} _{-0.01}	6.18 ^{+0.02} _{-0.02}	6.05 ^{+0.04} _{-0.04}	5.89 ^{+0.02} _{-0.02}	6.16 ^{+0.06} _{-0.06}	5.65 ^{+0.06} _{-0.06}
88.8	5.38 ^{+0.01} _{-0.01}	5.67 ^{+0.01} _{-0.01}	6.11 ^{+0.02} _{-0.02}	5.99 ^{+0.05} _{-0.05}	5.81 ^{+0.02} _{-0.02}	6.08 ^{+0.05} _{-0.05}	5.58 ^{+0.05} _{-0.05}
97.2	5.29 ^{+0.01} _{-0.01}	5.56 ^{+0.01} _{-0.01}	5.98 ^{+0.02} _{-0.02}	5.92 ^{+0.04} _{-0.04}	5.69 ^{+0.02} _{-0.02}	5.99 ^{+0.05} _{-0.05}	5.47 ^{+0.05} _{-0.05}
103.6	5.21 ^{+0.01} _{-0.01}	5.49 ^{+0.01} _{-0.01}	5.89 ^{+0.03} _{-0.03}	5.84 ^{+0.05} _{-0.05}	5.62 ^{+0.02} _{-0.02}	5.94 ^{+0.05} _{-0.05}	5.39 ^{+0.05} _{-0.05}
111.6	5.14 ^{+0.01} _{-0.01}	5.40 ^{+0.01} _{-0.01}	5.79 ^{+0.03} _{-0.03}	5.78 ^{+0.05} _{-0.05}	5.54 ^{+0.02} _{-0.02}	5.87 ^{+0.05} _{-0.05}	5.32 ^{+0.05} _{-0.05}
117.2	5.10 ^{+0.01} _{-0.01}	5.36 ^{+0.01} _{-0.01}	5.72 ^{+0.03} _{-0.03}	5.72 ^{+0.05} _{-0.05}	5.47 ^{+0.02} _{-0.02}	5.82 ^{+0.05} _{-0.05}	5.29 ^{+0.05} _{-0.05}
129.0	5.00 ^{+0.01} _{-0.01}	5.25 ^{+0.02} _{-0.02}	5.61 ^{+0.03} _{-0.03}	5.64 ^{+0.05} _{-0.05}	5.36 ^{+0.02} _{-0.02}	5.74 ^{+0.05} _{-0.05}	5.21 ^{+0.05} _{-0.05}
141.7	4.89 ^{+0.02} _{-0.02}	5.13 ^{+0.02} _{-0.02}	5.49 ^{+0.03} _{-0.03}	5.58 ^{+0.05} _{-0.05}	5.23 ^{+0.03} _{-0.03}	5.66 ^{+0.05} _{-0.05}	5.09 ^{+0.05} _{-0.05}
146.7	4.85 ^{+0.02} _{-0.02}	5.10 ^{+0.02} _{-0.02}	5.46 ^{+0.03} _{-0.03}	5.51 ^{+0.06} _{-0.06}	5.19 ^{+0.03} _{-0.03}	5.61 ^{+0.05} _{-0.05}	5.03 ^{+0.05} _{-0.05}

Note. — Average μ_\star profiles of massive cenHighMh and cenLowMh galaxies in different samples:

Col. (1) Radius along the major axis in kpc.

Col. (2) Average μ_\star profile for galaxies with $11.4 \leq \log(M_{\star,100\text{kpc}}/M_\odot) < 11.6$ in the combined samples of cenHighMh and cenLowMh galaxies.

Col. (3) Average μ_\star profile of combined samples in the mass bin of $11.6 \leq \log(M_{\star,100\text{kpc}}/M_\odot) < 11.8$.

Col. (4) Average μ_\star profile of combined samples in the mass bin of $11.8 \leq \log(M_{\star,100\text{kpc}}/M_\odot) < 12.0$.

Col. (5) and Col. (6) are the average μ_\star profiles of cenHighMh and cenLowMh galaxies in the $M_{\star,100\text{kpc}}$ -matched samples within $11.6 \leq \log(M_{\star,100\text{kpc}}/M_\odot) < 11.9$.

Col. (7) and Col. (8) are the average μ_\star profiles of cenHighMh and cenLowMh galaxies in the $M_{\star,10\text{kpc}}$ -matched samples within $11.2 \leq \log(M_{\star,10\text{kpc}}/M_\odot) < 11.6$.

The upper and lower uncertainties of these average profiles via bootstrap-resampling method are also displayed.